

LevelSetPy: A GPU-Accelerated Package for Resolving Hyperbolic Hamilton-Jacobi Partial Differential Equations

LEKAN MOLU, Microsoft Research, USA

Verification and safety analyses of the systems that we design has become timely given the complexity of modern systems across the various fronts of the sciences and engineering. It is well-known that the terminal value function of hyperbolic Hamilton-Jacobi (HJ) partial differential equations (PDEs) can serve as a reliably accurate surrogate for systems verification. This technical document is devoted to several themes surrounding the numerical solutions to hyperbolic HJ PDEs (which often do not admit closed-form solutions) *viz.*, their implicit representation (as interfaces) on co-dimension one domains; dynamics evolution with levelsets; unwinding spatial derivatives; total variation diminishing Runge-Kutta integration schemes via method of lines; and their applications to the theory of reachable sets and safety-critical systems analyses. The Cauchy-type HJ evolution equation and its level set *dynamics* that we chiefly consider are increasingly finding interest in multiple research domains including (a) analyzing safety-critical problems in reinforcement learning, and broadly in robotics and automation; (b) control engineering; (c) computing flows in transport problems; (d) aerospace and defense engineering domains; (e) geometric optics; (f) volume of fluid analysis; and (g) image processing *inter alia*. We briefly review HJ theory and its viscosity approximations, describe a hierarchy of library components, and provide rigorously-tested representative numerical examples in reachability differential games, transport analysis, and time-optimal control problems. This GPU software package allows for easy portability and extensibility to modern libraries for the analyses of safety-critical algorithms in (reinforcement) learning, control, robotics, transport, and flow problems *inter alia*. In addition, we provide a CPU implementation in python that is significantly faster and more useful than existing alternatives. The various implementations we have written allow easy extensibility of safety and verification analysis on modern computer architectures. Let us enquire.

CCS Concepts: • **Software and its engineering** → **Software libraries and repositories**; • **Applied computing** → **Physical sciences and engineering**; • **Mathematics of computing** → **Solvers**.

Additional Key Words and Phrases: partial differential equations, level sets, reachability theory

ACM Reference Format:

Lekan Molu. 20XX. LevelSetPy: A GPU-Accelerated Package for Resolving Hyperbolic Hamilton-Jacobi Partial Differential Equations. *J. ACM* 00, 0, Article 000 (20XX), 35 pages. <https://doi.org/XXXXXXX.XXXXXXX>

1 OVERVIEW

The need for scalable and faster numerical algorithms in software for *verifying* and *validating* systems has become timely given the emerging growth of complexity in the systems that we design and build. That which entails generating evidence that a system or one or more of its components satisfy all specified requirements and functional and allocated baselines is termed verification [13]. Whereas, validation entails providing unprovable evidence that system capabilities comply with an end-user's performance requirements and satisfies its intended operational environment [12]. We focus on verification in this article. This is commonly referred to as safety (ascertaining the

Author's address: Lekan Molu, lekanmolu@microsoft.com, Microsoft Research, 300 Lafayette Street, New York, NY, USA, 10012.

Permission to make digital or hard copies of all or part of this work for personal or classroom use is granted without fee provided that copies are not made or distributed for profit or commercial advantage and that copies bear this notice and the full citation on the first page. Copyrights for components of this work owned by others than ACM must be honored. Abstracting with credit is permitted. To copy otherwise, or republish, to post on servers or to redistribute to lists, requires prior specific permission and/or a fee. Request permissions from permissions@acm.org.

© 20XX Association for Computing Machinery.

0004-5411/20XX/0-ART000 \$15.00

<https://doi.org/XXXXXXX.XXXXXXX>

freedom of a system from harm) in software design and programming language, aerospace and defense, as well as control theory literature. For the rest of this article safety shall be taken to mean verification. The foremost open-source verification software for engineering applications based on Hamilton-Jacobi equations [17, 28] and level set methods [37, 42] is the CPU-based MATLAB® [33] level sets toolbox, written in 2005 A.D. before the era of graphical processing units (GPU)-accelerated computations. Since, there has been a lot of improvement in computing hardware design, architecture, and code-acceleration. This paper principally describes a GPU-accelerated software package – written entirely in python and accelerated on graphical processing units (GPUs) – for numerically resolving generalized discontinuous solutions to Cauchy-type (or time-dependent) Hamilton-Jacobi (HJ) hyperbolic partial differential equations (PDE 's) that arise in many problem contexts including (multi-agent) reinforcement learning, robotics, control theory, differential games, as well as flow and transport phenomena *inter alia*.

Accompanying the package are implicit calculus operations on dynamic codimension-one implicit interfaces embedded on surfaces in \mathbb{R}^n , and numerical (spatial and temporal) discretization schemes for hyperbolic partial differential equations. Furthermore, we describe explicit integration schemes including Lax-Friedrichs, Courant-Friedrichs-Lewy (CFL) integration TVD-RK conditioning schemes for HJ Hamiltonians of the form $H(\mathbf{x}, \mathbf{p})$, where \mathbf{x} is the state and \mathbf{p} is the co-state. Finally, extensions to reachability analyses for continuous and hybrid systems, formulated as optimal control or game theory problems using viscosity solutions to HJ PDE 's is described. While our emphasis is on the resolution of safe sets in a reachability context for verification settings, the applications of the software package herewith presented extend beyond control engineering applications.

The GPU package is available on the author's github repository: [LevelSetPy](#). The CPU implementation (in Python) can be found at [on the cpu-numpy tree of LevelSetPy](#). In addition, installation instructions are available on the github repository.

2 BACKGROUND AND MOTIVATION

Our chief interest is the evolution form of the HJ equation

$$\begin{aligned} v_t(\mathbf{x}, t) + H(t; \mathbf{x}, \nabla_{\mathbf{x}} v) &= 0 \text{ in } \Omega \times (0, T] \\ v(\mathbf{x}, t) &= g, \text{ on } \partial\Omega \times \{t = T\}, v(\mathbf{x}, 0) = v_0(\mathbf{x}) \text{ in } \Omega \end{aligned} \quad (1)$$

or the convection equation

$$\begin{aligned} v_t + \sum_{i=0}^N f_i(u)_{x_i} &= 0, \text{ for } t > 0, \mathbf{x} \in \mathbb{R}^n, \\ v(\mathbf{x}, 0) &= v_0(\mathbf{x}), \mathbf{x} \in \mathbb{R}^n \end{aligned} \quad (2)$$

where Ω is an open set in \mathbb{R}^n ; \mathbf{x} is the state; v_t denotes the partial derivative(s) of the solution v with respect to time t ; the Hamiltonian $H : (0, T] \times \mathbb{R}^n \times \mathbb{R}^n \rightarrow \mathbb{R}$ and f are continuous; g , and v_0 are bounded and uniformly continuous (BUC) functions in \mathbb{R}^n ; and $\nabla_{\mathbf{x}} v$ is the spatial gradient of v . It is assumed that g and v_0 are given.

Solving problems described by (1) under appropriate boundary and/or initial conditions using the method of characteristics is limiting as a result of crossing characteristics [9]. In the same vein, global analysis is virtually impossible owing to the lack of existence and uniqueness of solutions $v \in C^1(\Omega) \times (0, T]$ even if H and g are smooth [9].

The method of “vanishing viscosity”, based on the idea of traversing the limit as $\delta \rightarrow 0$ in the hyperbolic equation (1) (where a parameter $\delta > 0$ “endows” the problem in a viscosity sense as in gas dynamics [23]), allows generalized (discontinuous) solutions [15] whereupon if $v \in W_{loc}^{1,\infty}(\Omega) \times (0, T]$ and $H \in W_{loc}^{1,\infty}(\Omega)$, one can lay claim to strong notions of general existence, stability, and uniqueness

to BUC solutions v^δ of the (approximate) viscous Cauchy-type HJ equation

$$\begin{aligned} v_t^\delta + H(t; x, \nabla_x v^\delta) - \delta \Delta v^\delta &= 0 \text{ in } \Omega \times (0, T] \\ v^\delta(x, t) &= g, \text{ on } \partial\Omega \times \{t = T\}, v^\delta(x, 0) = v_0(x) \text{ in } \Omega \end{aligned} \quad (3)$$

in the class $BUC(\Omega \times [0, T]) \cap C^{2,1}(\Omega \times (0, T])$ i.e. continuous second-order spatial and first order time derivatives for all time $T < \infty$. Crandall and Lions [10] showed that $|v^\delta(x, t) - v(x, t)| \leq k\sqrt{\delta}$ for $x \in \Omega$ and $t > 0$. For most of this article, we are concerned with *generalized* viscosity solutions of the manner described by (3).

Popular means of computing the solution v^δ of (3) leverage hyperbolic conservation laws in generating *propagation of surfaces under curvature* (PSC) [38]. These PSC algorithms *implicitly* embed $(n - 1)$ dimensional *interfaces* (or isocontours) between two or more separable regions in spatial dimensions belonging in \mathbb{R}^n . The interface's speed is typically set as a function of the dynamical system's curvature, and the front gets passively advected by a coupled flow.

This implicit representation has found solution in a wide array of flow/motion of many physical phenomena such as gas dynamics, global illumination problems, and problems arising in the evolution of the trajectories of dynamical systems in a reachable control context [32, 34, 35]. These schemes work despite these phenomena developing discontinuities, corners, or cusps as dynamics evolve owing to the rich theory of viscosity solutions to HJ problems [8, 9, 15, 29].

Mitchell [35] connected techniques used in level set methods to reachability analysis in optimal control, essentially showing that the zero-level set of the differential zero-sum two-person game in an Hamilton-Jacobi-Isaacs (HJI) setting [15, 24] constitutes the safe set of a reachability problem. Reachability concerns evaluating the *decidability* of a dynamical system's trajectories' evolution throughout a state space. Decidable reachable systems are those where one can compute all states that can be reached from an initial condition in a *finite number of steps*. For inf-sup or sup-inf optimal control problems [30], the Hamiltonian is related to the *backward* reachable set of a dynamical system. The essential fabric of this technical communique revolves around reachability problems defined on co-dimension-one surfaces.

The well-known `LevelSet Toolbox` [33] is the consolidated `MATLAB®` package that contains the gridding methods, boundary conditions, time and spatial derivatives, integrators and helper functions. While Mitchell motivated the execution of the toolkit in `MATLAB®` for the expressiveness the language provides, modern data manipulation and scripting libraries often render the original package non-portable across distributed hardware since it lacks other programming language interoperability, particularly python and its associated scientific computing libraries such as `Numpy`, `Scipy`, `PyTorch` and their variants.

In this regard, we revisit the major algorithms necessary for implicit surface representation of HJ PDEs, write the spatial, temporal, and monotone difference schemes in Python, accelerated onto GPUs via `CuPy` [36] and present representative numerical examples.

2.1 Contributions

Given the prevalence of HJ PDEs in application areas encompassing robotics and learning-enabled (control) systems, the need for easy portability and extensibility to other popular software packages has necessitated our rewriting the toolbox in a single python package, leveraging GPU computations, and covering the essential algorithms of Crandall [11], Osher and Fedkiw [37], and Mitchell [33]. Our contributions are as follows:

- (1) we describe the details of the `LevelSetPy` software, starting with the common implicit surfaces that are used as initial conditions to represent $v(x, t)$ leveraging signed distance functions (SDF) and the associated boolean operations and calculus toolboxes for their *dynamics* endowment;

- (2) we describe the upwinding spatial derivative schemes, temporal discretization via method of lines schemes based on (approximate) total variation diminishing (TVD) Runge-Kutta (RK), and stabilizing Lax-Friedrichs schemes for multidimensional monotone Hamiltonians of HJ equations or scalar conservation laws;
- (3) we conclude this article with three representative examples, viz., (i) the barrier surface for two adversarial rockets traveling on a plane; (ii) the time-to-reach time-optimal control problem for a generic double integrator system; and (iii) analyze the barrier surface for a flock of birds traversing a phase space.

This article provides a description of the underlying theory and implementation of these hyperbolic PDE's. First, in section 3, differential games in the context of dynamic programming and reachability theory are introduced. Second, in section 4, we describe the geometry of (and Boolean operations on) implicit function representations of continuous-time value functions described by (1) using Cartesian grids. Third, spatial derivatives to scalar conservation laws are described in section 5, and temporal discretization schemes for these conservation laws follow thereafter. Fourth, in section 7 we describe real-world problems and make them amenable to HJ PDE's and the construction of safe sets or tubes within a verification geometrical reasoning framework: we present numerical results on the motivated examples to demonstrate the efficacy of our software package on diverse representative problems that cover time-to-reach optimal control, and HJI differential games in reachability settings. Sixth, we conclude the paper in section 8. Additional examples, `jupyter` notebooks, and representative problems are provided in the online package.

3 DIFFERENTIAL GAMES AND REACHABILITY

In this section, we briefly describe reachability theory within the context of the HJ-Isaacs (HJI) equation [24]. Reachable sets in the context of two person games is introduced. We then establish the “viscuous” PDE to the terminal HJI PDE.

For a state $\mathbf{x} \in \Omega$, fix: $T > t \geq 0$. Suppose that the controls for opposing players P and E in a two-player differential game are given by measurable functions

$$\mathbf{u} : [t, T] \rightarrow \mathcal{U}, \quad \mathbf{w} : [t, T] \rightarrow \mathcal{W} \quad (4)$$

where $\mathcal{U} \in \mathbb{R}^m$ and $\mathcal{W} \subset \mathbb{R}^p$ are compact sets. Let us consider the differential equation,

$$\dot{\mathbf{x}}(\tau) = \mathbf{f}(\tau, \mathbf{x}(\tau), \mathbf{u}(\tau), \mathbf{w}(\tau)), t \leq \tau \leq T, \quad \mathbf{x}(t) = \mathbf{x}, \quad (5)$$

where $\mathbf{f}(\tau, \cdot, \cdot, \cdot)$ is uniformly continuous and $\mathbf{x}(\cdot)$ is the unique solution of system (5). Suppose that we associate with the dynamical system (5) the payoff functional

$$\Phi(t; \mathbf{x}, \mathbf{u}, \mathbf{w}) = \int_t^T \mathbf{l}(\tau, \mathbf{x}(\tau), \mathbf{u}(\tau), \mathbf{w}(\tau)) d\tau + \mathbf{g}(\mathbf{x}(T)), \quad (6)$$

where $\mathbf{g} : \mathbb{R}^n \rightarrow \mathbb{R}$ satisfies

$$|\mathbf{g}(\mathbf{x})| \leq k_1, \quad |\mathbf{g}(\mathbf{x}) - \mathbf{g}(\hat{\mathbf{x}})| \leq k_1 |\mathbf{x} - \hat{\mathbf{x}}| \quad (7a)$$

and $\mathbf{l} : [0, T] \times \mathbb{R}^n \times \mathcal{U} \times \mathcal{W} \rightarrow \mathbb{R}$ is the BUC stage cost. We say T is the *terminal time* (it may be infinity!) and the integral, when it does not depend on the control laws, is the *performance index*. The evader is maximizing and pursuer is minimizing the payoff (6). In reachability analysis, the cost-to-go $\mathbf{l}(\cdot)$ is taken as zero so that the payoff functional (6) becomes

$$\Phi(t; \mathbf{x}, \mathbf{u}, \mathbf{w}) = \mathbf{g}(\mathbf{x}(T)). \quad (8)$$

3.1 HJI's Lower Value and its Viscosity Solution

Define

$$\bar{\mathcal{U}} \equiv \{u : [t, T] \rightarrow \mathcal{U}\} \text{ and } \bar{\mathcal{W}} \equiv \{w : [t, T] \rightarrow \mathcal{W}\} \quad (9)$$

as all control sets for players P and E . For controls which agree almost everywhere (a.e.), we are interested in the pursuer's mapping strategy (starting at t) i.e.

$$\beta : \bar{\mathcal{U}}(t) \rightarrow \bar{\mathcal{W}}(t) \quad (10)$$

provided for each $t \leq \tau \leq T$ and $u, \hat{u} \in \bar{\mathcal{U}}(t)$; then $u(\bar{t}) = \hat{u}(\bar{t})$ a.e. on $t \leq \bar{t} \leq \tau$ implies $\beta[u](\bar{t}) = \beta[\hat{u}](\bar{t})$ a.e. on $t \leq \bar{t} \leq \tau$. The differential game's *lower value* for a solution $x(t)$ of (5) for a $u(t)$ and $w(t) = \beta[u](\cdot)$ is [16]

$$\begin{aligned} v(x, t) &= \inf_{\beta \in \mathcal{B}(t)} \sup_{u \in \bar{\mathcal{U}}(t)} \Phi(t, x, u, \beta[u]) \\ &= \inf_{\beta \in \mathcal{B}(t)} \sup_{u \in \bar{\mathcal{U}}(t)} g(x(T)). \end{aligned} \quad (11)$$

We say $v(x, t)$ is the lower value function of the differential game. This value function is used in backward reachability analysis, the chief subject of our discourse.

LEMMA 1. *The lower value $v(x, t)$ in (11) is the viscosity solution to the lower Hamilton-Jacobi Isaac's equation (1) and it has with it the lower Hamiltonian,*

$$H(t, x, u, w, p) = \max_{u \in \mathcal{U}} \min_{w \in \mathcal{V}} \langle f(t, x, u, w), p \rangle. \quad (12)$$

where p is the co-state, i.e. the spatial derivative of v w.r.t x and $\langle \cdot, \cdot \rangle$ is the dot product operator between two variables.

PROOF. This proof is given in [16]. □

3.2 Optimal Control, HJI PDE, and Reachability Theory

That which concerns point sets for a dynamical system's behavioral evolution (or trajectory) throughout a phase space¹ and such that the sets satisfy input or state constraints in a least restrictive sense and under a worst-possible disturbance [30] describes reachability. For computational and decidability reasons², we restrict our computation scheme over a finite time period. This is a classic reachability theory problem.

Reachability analysis is concerned with finding the set of forward (resp. backward) states that are reachable from a set of initial (resp. target) state sets, *up to a final time* under the worst possible disturbance. This verification problem usually consists in finding a *reachable states set* that lie along the trajectory of the solution to a first order nonlinear P.D.E. Typically, this solution originates from some initial phase (x_0, t_0) up to a state, $x(T)$, at a specified final time T . Once computed, the optimal value function provides a safety certificate and controller defined by the spatial gradients of the value function.

In addition to producing a value function, the optimality principle of dynamic programming on the underlying HJI PDE can be used to generate a minimum time-to-reach (TTR) function. This function maps initial conditions to the minimum time horizon required to reach the target set. This can be computed by "stacking" the zero level sets of the value function as it propagates backwards in time [1, 3, 34].

¹To avoid the cumbersome phrase "the state x at time t ", we will associate the pair (x, t) with the *phase* of the system for a state x at time t . We associate the Cartesian product of Ω and the space $T = \mathbb{R}^1$ of all time values as the *phase space* of $\Omega \times T$.

²We say a reachability problem is decidable if we can compute all the states that can be reached from an initial condition in a finite number of steps.

Backward reachable sets (within a continuous system framework) are those subsets of a phase space whereupon trajectories initialized in some subset of the phase space can reach a so-called target set, $\mathcal{L}(x)$. Mitchell et. al' [35] essential contribution was that viscosity solution of the Cauchy-type HJI PDE (1) or (12) is tantamount to an implicit surface representation of the continuous-time backward reachable set. This formulation is amenable to modern large-scale problems because level set methods can be used in computing the target set as the viscosity solution is numerically continuous everywhere and well-posed. In backward reachability analysis, the ordering of time indices is reversed so that instead of having $t \in [0, T]$, we shall henceforth have $t \in [-T, 0]$.

3.3 The Backward Reachable (Target) Set

Suppose that the goal for an agent moving over a phase space is to reach a region at the end of a time horizon. We could leverage the terminal cost $g(\cdot)$ in (12) and impose constraints

$$|g(0; x)| \leq k, \quad |g(0; x) - g(t; \hat{x})| \leq k|x - \hat{x}| \quad (13)$$

for constant k and all $-T \leq t \leq 0$, $\hat{x}, x \in \mathbb{R}^n$. The set

$$\mathcal{L}_0 = \{x \in \bar{\Omega} \mid g(0; x) \leq 0\}, \quad (14)$$

is called the *target set* (otherwise referred to as the backward reachable set) in the phase space $\Omega \times \mathbb{R}$ (proof in [35]). This target set can represent the failure set (to avoid) or a goal set (to reach) in the state space. Note that the target set, \mathcal{L}_0 , is a closed subset of \mathbb{R}^n and is in the closure of Ω . Typically \mathcal{L}_0 is user-defined, and in level set methods, $g(x)$ is a signed distance function – negative inside the target set and positive elsewhere.

3.4 The Backward Reachable Tube

It is often desirable to consider all conditions under which trajectories of the system may enter a user-defined target set. This could be desirable in goal-regions of the phase space (safe sets) or undesirable configurations (unsafe sets).

For the safety problem setup in (11), we can define the corresponding *robustly controlled backward reachable tube* [34] as the closure of the open set

$$\mathcal{L}([\tau, 0], \mathcal{L}_0) = \{x \in \Omega \mid \exists \beta \in \bar{\mathcal{W}}(t) \forall u \in \mathcal{U}(t), \exists \tau \in [-T, 0], \xi(\bar{t}) \in \mathcal{L}_0\}. \quad (15)$$

Read: The set of states from which the strategies of P and for all controls of E imply that we *reach and remain in the target set* in the interval $[-T, 0]$. Following Lemma 2 of [35], the states in the reachable set admit the following properties w.r.t the value function v :

$$x(t) \in \mathcal{L}(\cdot) \implies v(x, t) \leq 0, \quad (16a)$$

$$v(x, t) \leq 0 \implies x(t) \in \mathcal{L}(\cdot). \quad (16b)$$

Player P is minimizing (the game's termination time c.f. (14)), seeking to drive system trajectories into the unsafe set; and player E is maximizing (the game's termination time) i.e. is seeking to avoid the unsafe set³.

4 GEOMETRY OF IMPLICIT SURFACES AND LAYOUTS

In this section, we discuss how implicit surface functions are constructed, stored on local memory and how they are transferred to GPUs. Throughout, links to `api's`, `routines`, and `subroutines`

³For the goal-satisfaction (or *liveness*) problem setups, the strategies are reversed and the backward reachable tube are the states from which the evader E can successfully reach the target set despite worst-case efforts of the pursuer P .

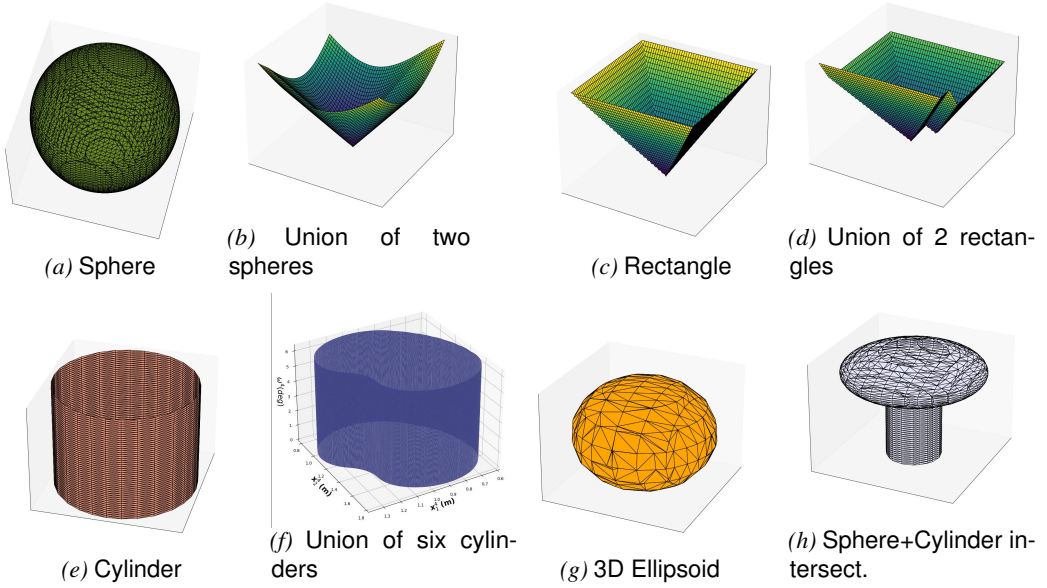


Fig. 1. Examples of implicitly constructed zero levelsets of interfaces of geometric primitives along with Boolean operations on 2D and 3D Cartesian grids. Zero level set of (a) a sphere on a 3D grid; (b) union of two 3D spheres implicitly constructed on a 2D grid; (c) a rectangle on a 2D grid; (d) the union of rectangles on a 2D grid; (e) a cylinder on a 3D grid; (f) the union of multiple cylinders on a 3D grid; (g) an ellipsoid on a 3D grid; (h) Intersection of a sphere and a cylinder on a 3D grid.

are highlighted in [blue text](#) (with a working hyperlink) and we use code snippets in Python to illustrate API calls when it's convenient.

In what follows in this section, at issue are functions $f(x)$ for points x that do not explicitly describe but rather imply the existence of f . This representation is attractive since it requires less number of points to represent a function than explicit forms. Let us describe the representation of data we employ in what follows.

4.1 Grids Layout

Fundamental to implicit surface representations are Cartesian grids in our library. Packages that implement 'grid' data structures are in the folder [Grids](#). Grid **g** is [created](#) by specifying minimum, \mathbf{g}_{min} , and maximum axes bounds, \mathbf{g}_{max} , along every Cartesian coordinate axes n (see lines 3 and 4) of Listing 1; a desired number of discrete points N is passed to the grid data structure – specifying the number of grid nodes and the grid spacing in each dimension as (line 5) listed in Listing 1. On line 5, a grid data structure is constructed and all input parameters to the API are checked for consistency. The contents of the grid data structure are fully described in Definition 1.

```

1  from math import pi
2  import numpy as np
3  gmin = np.array((-5, -5, -pi)) // lower corner
4  gmax = np.array((5, 5, pi)) // upper corner
5  N = 41*ones(3, 1) // number of grid nodes
6  pdim = 3; // periodic boundary condition, dim 3
7  g = createGrid(gmin, gmax, N, pdim)

```

Listing 1. Creating a three-dimensional grid.

DEFINITION 1 (GRID DATA STRUCTURE). A grid *data structure*, \mathbf{g} , (implemented in Listing 1) has the following fields: (i) discretized nodes of the state(s) x in (3), denoted as 1-D vectors $\mathbf{g}.vs$; (ii) given the 1-D vectors $\mathbf{g}.vs$, an n -dimensional array of coordinates over n -dimensional grids is computed with matrix-based indexing; this generates a mesh for all state nodal points on the grid $\mathbf{g}.xs$ as a list across all the dimensions of the grid; (iii) grid dimension $\mathbf{g}.dim$, denoting the number of Cartesian axes needed for representing the state x^4 ; (iv) boundary conditions of the relevant HJ equation to be solved are grafted in by populating the corresponding grid dimension with ghost cells (to be introduced shortly).

4.2 Implicit Surface Representations: Levelsets

For an implicit surface representation of a geometric function, we treat the coordinates as functional arguments instead of functional values using a fixed level set of continuous function $\mathbf{v} : \mathbb{R}^n \rightarrow \mathbb{R}$. We use signed distance functions to represent moving fronts throughout. When the signed distance function is not numerically possible, we describe where the implicit surface representations are smeared out in every routines' documentation.

The query points for moving interfaces are grid point sets of the computational domain described by implicit geometric primitives such as spheres, cylinders, ellipsoids and even polyhedrons such as icosahedrons. All of these are contained in the folder [InitialConditions](#) on our projects page.

Suppose that the zero levelset of an implicit surface $\mathbf{v}(x, t)$ is defined as $\Gamma = \{x : \mathbf{v}(x) = 0\}$ on a grid $G \in \mathbb{R}^n$, where n denotes the number of dimensions. Our representation of Γ on G generalizes a row-major layout. An example representation of an ellipsoid on a three-dimensional grid is illustrated in Listing 2.

```

1 e = (g.xs[0])**2 // ellipsoid nodal points
2 e += 4.0*(g.xs[1])**2
3 if g.dim==3:
4     data += (9.0*(g.xs[2])**2)
5 e -= radius // radius=major axis of ellipsoid

```

Listing 2. An ellipsoid as a signed distance function.

4.3 Calculus on Implicit Function Representations

Geometrical operations on implicitly defined functions carries through in the package as follows.

Suppose that $\mathbf{v}_1(x)$ and $\mathbf{v}_2(x)$ are two signed distance representations, then the union of the interior of the two functions is simply $\min(\mathbf{v}_1(x), \mathbf{v}_2(x))$ (example illustrations in Fig. 1 a, c, d and h). The intersection of the interior of two signed distance functions is generated by $\max(\mathbf{v}_1(x), \mathbf{v}_2(x))$ (example illustrations in Fig. 1). The complement of a function is found by negating its signed distance function i.e. $-\mathbf{v}(x)$. The resultant function as a result of the subtraction of the interior of one signed distance function \mathbf{v}_2 from the another one, say, \mathbf{v}_1 is defined $\max(\mathbf{v}_1(x), -\mathbf{v}_2(x))$. All of these are implemented in the module [shapeOps](#).

5 SPATIAL DISCRETIZATION: UPWINDING

Monotone solutions to the levelset equation, as introduced by Crandall and Lions [10] are attractive but they are at most first-order accurate and tend to be dissipative for most practical applications. In this section, we discuss higher-order upwinding schemes that mimic high-order essentially non-oscillatory (ENO) schemes for computing the spatial derivatives \mathbf{v}_x for the numerical viscosity

⁴This parameter is useful when computing signed distance to every nodal point on the state space in the implicit representation of \mathbf{v}

solutions to levelset PDE's of the *Eulerian form* (introduced in (17)). Codebases for procedures herewith described are in the folder `SpatialDerivatives`.

Using the Eulerian form of the levelset equation,

$$\mathbf{v}_t + \mathbf{F} \cdot \nabla \mathbf{v} = 0 \quad (17)$$

where \mathbf{F} is the speed function, the implicit function itself (section 4) is used both to denote and to evolve the interface. Suppose that the interface speed \mathbf{F} is a three-vector $[f_x, f_y, f_z]$ on a three-dimensional Cartesian grid, expanding (17) the evolution of the implicit function on the zero levelset yields the Eulerian form

$$\mathbf{v}_t + f_x \mathbf{v}_x + f_y \mathbf{v}_y + f_z \mathbf{v}_z = 0 \quad (18)$$

of the interface evolution given that the interface encapsulates the implicit representation \mathbf{v} . In our implementations, we define \mathbf{v} throughout the computational domain Ω . However, narrow band methods [41] that only contain the interface can be implemented as well so that memory is saved while the front is being tracked. -

5.1 Upwinding

Let us first define the following differencing schemes

$$D^- \mathbf{v} = \frac{\partial \mathbf{v}}{\partial x} \approx \frac{\mathbf{v}_{i+1} - \mathbf{v}_i}{\Delta x}, D^+ \mathbf{v} \approx \frac{\mathbf{v}_i - \mathbf{v}_{i-1}}{\Delta x}. \quad (19)$$

Suppose that \mathbf{v} and its speed \mathbf{F} are defined over a domain Ω (this is the Cartesian grid in our representation). Using the forward Euler method, the levelset equation (18) becomes

$$\frac{\mathbf{v}^{n+1} - \mathbf{v}^n}{\Delta t} + f_x^n \mathbf{v}_x^n + f_y^n \mathbf{v}_y^n + f_z^n \mathbf{v}_z^n = 0. \quad (20)$$

Now, suppose that we are on a one-dimensional surface and around a grid point i , then given that f^n may be spatially varying the equation in the foregoing evaluates to

$$\frac{\mathbf{v}_i^{n+1} - \mathbf{v}_i^n}{\Delta t} + f_i^n (\mathbf{v}_x)_i^n = 0 \quad (21)$$

where $(\mathbf{v}_x)_i$ denotes the spatial derivative of \mathbf{v} w.r.t x at the point i .

5.2 First-order accurate discretization

If $f_i > 0$, the values of \mathbf{v} are traversing from left to right so that in order to update \mathbf{v} at the end of the next time step, we must look to the left (going by the method of characteristics [37, §3.1]) and vice versa if $f_i < 0$. We therefore follow the standard upwinding method by using (19): we approximate \mathbf{v}_x with $D^- \mathbf{v}$ whenever $f_i > 0$ and we approximate \mathbf{v}_x with $D^+ \mathbf{v}$ whenever $f_i < 0$. No approximation is needed when $f_i = 0$ since $f_i (\mathbf{v}_x)_i$ vanishes. This discretization scheme is accurate within $O(\Delta x)$ given the first order accurate approximations $D^- \mathbf{v}$ and $D^+ \mathbf{v}$. We have followed the naming convention in [33] and in our `SpatialDerivatives` folder, we name this function `upwindFirstFirst`.

5.3 ENO Polynomial Interpolation of Solutions

Using a divided difference table, essentially non-oscillatory (ENO) polynomial interpolation of the discretization [40] of the levelset equation are known to generate improved numerical approximations to $D^- \mathbf{v}$ and $D^+ \mathbf{v}$.

Suppose that we choose a uniform mesh discretization Δx . Define the zeroth divided differences of \mathbf{v} at the grid nodes i as

$$D_i^0 \mathbf{v} = \mathbf{v}_i, \quad (22)$$

and the first, second, and third order divided differences of \mathbf{v} as the midway between grid nodes i.e.

$$\begin{aligned} D_{i+1/2}^1 \mathbf{v} &= \frac{D_{i+1}^0 \mathbf{v} - D_i^0 \mathbf{v}}{\Delta x}, \quad D_i^2 \mathbf{v} = \frac{D_{i+1/2}^1 \mathbf{v} - D_{i-1/2}^1 \mathbf{v}}{2\Delta x}, \\ D_{i+1/2}^3 \mathbf{v} &= \frac{D_{i+1}^2 \mathbf{v} - D_i^2 \mathbf{v}}{3\Delta x}. \end{aligned} \quad (23)$$

Then, an essentially non-oscillating polynomial of the form

$$\mathbf{v}(x) = Q_0(x) + Q_1(x) + Q_2(x) + Q_3(x) \quad (24)$$

can be constructed. In this light, the backward and forward spatial derivatives of \mathbf{v} w.r.t x at grid node i is found in terms of the derivatives of the coefficients $Q_i(x)$ in the foregoing i.e.

$$\mathbf{v}_x(x_i) = Q_1'(x_i) + Q_2'(x_i) + Q_3'(x_i). \quad (25)$$

Define $k = i - 1$ and $k = i$ for \mathbf{v}_x^- and \mathbf{v}_x^+ respectively. Then the first order accurate polynomial interpolation is essentially

$$Q_1(x) = (D_{k+1/2}^1 \mathbf{v})(x - x_i), \quad Q_1'(x_i) = D_{k+1/2}^1 \mathbf{v} \quad (26)$$

i.e. first-order upwinding.

We follow [37]'s recommendation in avoiding interpolating near large oscillations in gradients. Therefore, we choose a constant c such that

$$c = \begin{cases} D_k^2 \mathbf{v} & \text{if } |D_k^2 \mathbf{v}| \leq |D_{k+1}^2 \mathbf{v}| \\ D_{k+1}^2 \mathbf{v} & \text{otherwise} \end{cases} \quad (27)$$

so that

$$Q_2(x) = c(x - x_k)(x - x_{k+1}), \quad (28a)$$

$$Q_2'(x_i) = c(2i - 2k - 1)\Delta x \quad (28b)$$

is the second-order accurate upwinding solution for the polynomial interpolation. This is implemented as `upwindFirstENO2` in the `SpatialDerivatives` folder.

To obtain a third-order accurate solution, we choose c^* as follows

$$c^* = \begin{cases} D_{k^*+1/2}^3 \mathbf{v} & \text{if } |D_{k^*+1/2}^3 \mathbf{v}| \leq |D_{k^*+3/2}^3 \mathbf{v}| \\ D_{k^*+3/2}^3 \mathbf{v} & \text{if } |D_{k^*+1/2}^3 \mathbf{v}| > |D_{k^*+3/2}^3 \mathbf{v}|. \end{cases} \quad (29)$$

Whence, we have

$$Q_3(x) = c^*(x - x_{k^*})(x - x_{k^*+1})(x - x_{k^*+2}) \quad (30a)$$

$$Q_3'(x_i) = c^*(3(i - k^*)^2 - 6(i - k^*) + 2)(\Delta x)^2 \quad (30b)$$

for the third-order accurate correction to the approximated upwinding scheme (24). This is implemented as a routine in `upwindFirstENO3aHelper` and called as `upwindFirstENO3` in the `SpatialDerivatives` folder.

5.4 HJ Weighted Essentially Nonoscillatory Solutions

Here, we focus on weighted ENO (WENO) schemes with the same stencil as the third-order ENO scheme but with accuracy reaching as high as fifth-order in the smooth parts of the solution. Results here presented closely follow the presentation of Jiang and Peng in [26]. These WENO schemes approximate spatial derivatives at integer grid points as opposed to at half-integer grid values as we did in the ENO schemes in the previous section.

The third-order accurate ENO scheme essentially employs one of three substencils on a grid, namely $\{i-3, i-2, \dots, i\}$, $\{i-2, i-1, \dots, i+1\}$, and $\{i-1, \dots, i+3\}$ on the stencils range $\{i-3, i-2, \dots, i+3\}$ in calculating spatial derivatives for v .

Suppose that the spatial derivative v_x is to be found using the left-leaning substencil: $\{i-3, i-2, \dots, i\}$, then the third-order ENO scheme chooses one from

$$v_{x,i}^{-,0} = \frac{1}{3}D^+v_{i-3} - \frac{7}{6}D^+v_{i-2} + \frac{11}{6}D^+v_{i-1} \quad (31a)$$

$$v_{x,i}^{-,1} = -\frac{1}{6}D^+v_{i-2} + \frac{5}{6}D^+v_{i-1} + \frac{1}{3}D^+v_i \quad (31b)$$

$$v_{x,i}^{-,2} = -\frac{1}{3}D^+v_{i-1} + \frac{5}{6}D^+v_i - \frac{1}{6}D^+v_{i+1} \quad (31c)$$

where $v_{x,i}^{-,p}$ denotes the third-order p 'th substencil to $v_x(x_i)$ for $p = 0, 1, 2$. The WENO approximation to $v_x(x_i)$ leverages a convex weighted average of the three substencils so that

$$v_{x,i}^- = w_0 v_{x,i}^{-,0} + w_1 v_{x,i}^{-,1} + w_2 v_{x,i}^{-,2}. \quad (32)$$

In smooth regions of the phase space, $w_0 = 0.1$, $w_1 = 0.6$, and $w_2 = 0.3$ yield the optimally accurate fifth order WENO approximation, we have for $v_{x,i}^-$

$$\begin{aligned} & \frac{1}{30}D^+v_{i-3} - \frac{13}{60}D^+v_{i-2} + \frac{47}{60}D^+v_{i-1} \\ & + \frac{9}{20}D^+v_i - \frac{1}{20}D^+v_{i+1} \end{aligned} \quad (33)$$

the fifth-order approximation $v_x(x_i)$ and provides the smallest truncation error on a six-point stencil.

To account for weights in non-smooth regions, however, the smoothness of the stencils (31) can be estimated as recommended in [37, §3.4] so that if

$$\alpha_1 = 0.1/(\sigma_1 + \epsilon)^2, \quad \alpha_2 = 0.6/(\sigma_2 + \epsilon)^2, \quad \alpha_3 = 0.1/(\sigma_3 + \epsilon)^2 \quad (34)$$

for

$$\begin{aligned} \sigma_1 &= \frac{13}{12}(D^+v_{i-3} - 2D^+v_{i-2} + D^+v_{i-1})^2 \\ &+ \frac{1}{4}(D^+v_{i-3} - 4D^+v_{i-2} + 3D^+v_{i-1})^2, \end{aligned} \quad (35a)$$

$$\begin{aligned} \sigma_2 &= \frac{13}{12}(D^+v_{i-2} - 2D^+v_{i-1} + D^+v_i)^2 \\ &+ \frac{1}{4}(D^+v_{i-2} - D^+v_i)^2, \end{aligned} \quad (35b)$$

$$\begin{aligned} \sigma_3 &= \frac{13}{12}(D^+v_{i-1} - 2D^+v_i + D^+v_{i+1})^2 \\ &+ \frac{1}{4}(3D^+v_{i-1} - 4D^+v_i + D^+v_{i+1})^2, \end{aligned} \quad (35c)$$

and

$$\epsilon = 10^{-6} \max\{D^+v_{i-3}, D^+v_{i-2}, D^+v_{i-1}, D^+v_i, D^+v_{i+1}\} + 10^{-99} \quad (36)$$

then, we may define the weights for the WENO scheme as

$$w_1 = \alpha_1 / \sum_{i=1}^3 \alpha_i, \quad w_2 = \alpha_2 / \sum_{i=1}^3 \alpha_i, \quad w_3 = \alpha_3 / \sum_{i=1}^3 \alpha_i. \quad (37)$$

which well approximates the optimal weights $w_0 = 0.1$, $w_1 = 0.6$ and $w_2 = 0.3$ for decently smooth σ_k that can be dominated by ϵ . This is implemented as a routine in `upwindFirstWENO5a` and called as `upwindFirstWENO5`.

5.5 Lax-Friedrichs Monotone Difference Schemes

We now describe a convergent monotone difference spatial approximation scheme for scalar conservation laws of the form

$$\begin{aligned} v_t + \sum_{i=1}^N f_i(v)_{x_i} &= 0 \text{ for } t > 0, \mathbf{x} = (x_1, \dots, x_N) \in \mathbb{R}^n \\ v(\mathbf{x}, 0) &= v_0(\mathbf{x}), \text{ for } \mathbf{x} \in \mathbb{R}^n \end{aligned} \quad (38)$$

Suppose that $N = 1$, let us define $\lambda_x = \Delta t / \Delta x$, $\Delta_x^+ = v_{j+1} - v_j$, and $\Delta_x^- = v_j - v_{j-1}$. Then at the n th time step, the Lax-Friedrichs scheme is [11]

$$v_j^{n+1} = v_j^n - \frac{\lambda_x}{2} \Delta_x^0 f(v_j^n) + \frac{1}{2} \Delta_x^+ \Delta_x^- v_j^n. \quad (39)$$

Furthermore, if we define the flux on the state space as

$$g(v_j, v_{j-1}) = \frac{f(v_j) + f(v_{j-1})}{2} - \frac{1}{2} \lambda_x (v_j - v_{j-1}), \quad (40)$$

we may write

$$v_j^{n+1} = v_j^n - \lambda_x^+ (v_j, v_{j-1}). \quad (41)$$

The Lax-Friedrichs scheme is monotone on the interval $[a, b]$ if the CFL condition

$$\lambda_x \max_{a \leq v \leq b} |f'(v)| \leq 1 \quad (42)$$

for $(a, b) > 0$ and the upwind differencing scheme for a nondecreasing f is

$$v_j^{n+1} = v_j^n - \lambda_x \Delta_x^+ f(v_{j-1}^n). \quad (43)$$

For a nonincreasing f , we have

$$v_j^{n+1} = v_j^n - \lambda_x \Delta_x^+ f(v_j^n). \quad (44)$$

Our Lax-Friedrichs implementation is in the [link](#).

6 TEMPORAL DISCRETIZATION: METHOD OF LINES

Here, we describe further improvements on the numerical derivatives of HJ equations by further improving the fifth order accurate HJ WENO schemes presented in section 5. We adopt the *method of lines* (MOL) used in converting the time-dependent PDE's to ODE's.

In the MOL, the spatial derivatives in the PDE are replaced with algebraic approximations (in our case, one of the ENO schemes earlier presented) so that spatial derivatives no longer explicitly depend on spatial independent variables. Whence, only time, the initial value variable, is left so that we end up with a system of ordinary differential equations (ODEs) that closely approximate the original PDE.

Our presentation here follows the total variation diminishing (TVD) Runge Kutta (RK) schemes with Courant-Friedrichs-Lewy (CFL) conditioning imposed for stability as presented in [39] and implemented in MATLAB® in [33].

6.1 Higher-Order TVD-RK Time Discretizations

To adopt the method of lines, the N -dimensional levelset representation of \mathbf{v} is first rolled into a 1-D vector and an adaptive integration step size, Δt , is chosen to guarantee stability following the recommendation in [43]. The forward Euler algorithm thus becomes

$$\mathbf{v}(x, t + \Delta t) = \mathbf{v}(x, t) + \Delta t \Upsilon(x, \mathbf{v}(x, t)) \quad (45)$$

where Υ is now the function to be integrated.

A standard MOL can then be applied for the integration similar to ODEs (we have followed [33]'s code layout to provide consistency for MATLAB users). Since the details of the implementation are described in [33], we here describe the function arguments and describe call signatures.

We implement TVD-RK MOL schemes up to third-order accurate forward Euler integration schemes and the calling signature is as described in Listing 3.

```
1 odeCFLx(schemeFunc, tspan, y0, options, schemeData)
```

Listing 3. CFL-constrained method of lines routines.

where x could be one of 1, 2, or 3 to indicate first-order accurate, second-order accurate, or third-order accurate TVD-RK scheme. `schemeFunc` is typically a one of the Lax-Friedrichs approximation routines (implemented as `termLaxFriedrichs`) in the folder `ExplicitIntegration/Term` that approximates the HJ equation based on dissipation functions (to be shortly introduced).

The first-order accurate TVD (it is total variation bounded [TVB] actually) together with the spatial discretization used for the PDE is equivalent to the forward Euler method. We implement this as `odeCFL1`.

The second-order accurate TVD-RK scheme follows the RK scheme by evolving the Euler step to $t^n + \Delta t$,

$$\frac{\mathbf{v}^{n+1} - \mathbf{v}^n}{\Delta t} + F^n \cdot \nabla \mathbf{v}^n = 0. \quad (46)$$

A following Euler step to $t^n + 2\Delta t$ follows such that

$$\frac{\mathbf{v}^{n+2} - \mathbf{v}^{n+1}}{\Delta t} + F^{n+1} \cdot \nabla \mathbf{v}^{n+1} = 0 \quad (47)$$

before a convex combination of the initial value function and the result of the preceding Euler steps is taken in the following averaging step

$$\mathbf{v}^{n+1} = \frac{1}{2} \{ \mathbf{v}^n + \mathbf{v}^{n+2} \}. \quad (48)$$

The equation in the foregoing produces the second-order accurate TVD approximation to \mathbf{v} at $t^n + \Delta t$, implemented as `odeCFL2`.

With the third-order accurate TVD-RK scheme, the first two advancements in forward Euler schemes are computed but with a different averaging scheme

$$\mathbf{v}^{n+1/2} = \frac{1}{4} \{ 3\mathbf{v}^n + \mathbf{v}^{n+2} \} \quad (49)$$

which averages the previous two solutions at $t^n + \frac{1}{2}\Delta t$. The third Euler advancement step to $t^n + \frac{3}{2}\Delta t$ is

$$\frac{\mathbf{v}^{n+\frac{3}{2}} - \mathbf{v}^{n+\frac{1}{2}}}{\Delta t} + F^{n+\frac{1}{2}} \cdot \nabla \mathbf{v}^{n+\frac{1}{2}} = 0 \quad (50)$$

together with the averaging scheme

$$\boldsymbol{v}^{n+1} = \frac{1}{3} \{ \boldsymbol{v}^n + 2\boldsymbol{v}^{n+\frac{3}{2}} \} \quad (51)$$

to produce a third-order accurate approximation to \boldsymbol{v} at time $t^n + \Delta t$, implemented as `odeCFL3`.

7 EXAMPLES AND NUMERICAL EXPERIMENTS

In this section, we will present problems motivated by real-world scenarios and amend them to HJ PDE forms where their numerical solutions can be resolved with our `LevelSetPy` toolbox. The problems that we consider belong in `transport`, `differential games`, and `time-to-reach` problem classes. The library has been tested on numerous problems; however, for the sake of brevity we will only report a few results. We report our findings on `transport`, `differential games`, and `time-to-reach` problems.

For the differential games that we consider, each local optimization episode within a game may be characterized as a pursuit *game*, Γ . And by a game, we do not necessarily refer to a single game, but rather a *collection of games*, $\Upsilon = \{\Gamma_1, \dots, \Gamma_g\}$. Such a game terminates when *capture* occurs, that is the distance between players falls below a predetermined threshold. Each player in a game shall constitute either a pursuer (P) or an evader (E). Let the cursory reader not interpret P or E as controlling a single agent. In our various numerical experiments, we are poised with one or several pursuers (enemies) or evaders (peaceful citizens). However, when P or E governs the behavior of but one agent, these symbols will denote the agent itself.

We must settle upon how best should P pursue E . Here, at every time instant, P possesses knowledge of his own and that of E 's position so that P knows how to regulate its various controlling variables with respect to E 's motion in an optimal fashion. This follows the mathematical layout in section 3.

The rest of this section introduces three different representative examples where real-world problems are adopted and amended to HJ PDE forms and whose solution we seek to numerically recover. First, we present two rockets in a pursuit-evasion game where the goal is for the evader to guard a territory and the pursuer's goal is to penetrate the boundary of the territory being guarded. Second, we describe a double integral dynamical system: the double integral plant is a simplified abstraction of many real-world force-control system e.g. those that obey Newton's second law of motion or the torque-inertia dynamics of a body with rotary dynamics. We provide the numerical enumeration of the solution to the analytical time to reach problem. Third, we describe a collective behavior system in natural starlings and we provide a mathematical abstraction that allows the computation of the collision-avoidance *safety envelope* that may then be used in e.g. runtime assurance (RTA) safety-critical controller [22]. RTA controllers act intelligently as a safety system between a real-world controller and the system to be controlled by providing a state monitoring scheme useful in intervening in the real-world where vulnerabilities to danger is a constant factor to be mitigated against. All the examples presented in this section can be found in the `Examples` folder of our online library.

7.1 Two Rockets in a Pursuit-Evasion Terminal Value Differential Game

We adopt the rocket launch problem of Dreyfus [14] and amend it to a differential game between two identical rockets, P and E , on an (x, z) cross-section of a Cartesian plane. We set out to compute the *usable part* of the boundary of the *approximate* terminal surface of a predefined target set over a time horizon (i.e. the target tube). This target tube is a terminal surface; it describes regions of the phase space where capture is avoided after a game terminates. A rocket's motion is dictated by the

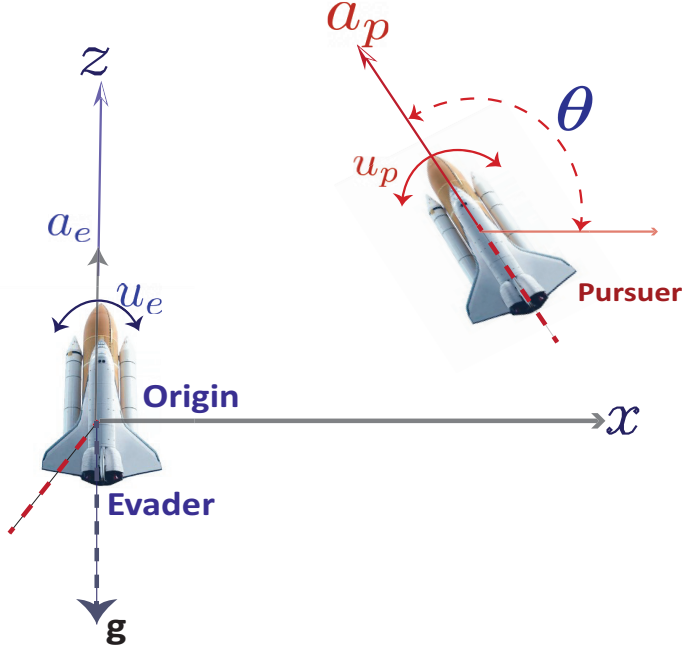


Fig. 2. Motion of two rockets on a Cartesian xz -plane with a thrust inclination in relative coordinates given by $\theta := u_p - u_e$.

following system of differential equations (under Dreyfus' assumptions):

$$\dot{x}_1 = x_3, \quad x_1(t_0) = 0; \quad (52a)$$

$$\dot{x}_2 = x_4, \quad x_2(t_0) = 0; \quad (52b)$$

$$\dot{x}_3 = a \cos u, \quad x_3(t_0) = 0; \quad (52c)$$

$$\dot{x}_4 = a \sin u - g, \quad x_4(t_0) = 0; \quad (52d)$$

where, (x_1, x_2) are respectively the horizontal and vertical range of the rocket (in feet); (x_3, x_4) are respectively the horizontal and vertical velocities of the rocket (in feet per second); and a and g are respectively the acceleration and gravitational accelerations (in feet per square second).

We now make the problem amenable to a two-player differential game analysis. The rockets P and E share identical dynamics in a general sense. The coordinates of P are freely chosen; however, the coordinates of E are chosen a distance ϕ away from (x, z) (at the origin of the plane) so that the PE vector's inclination measured counterclockwise from the x axis is θ as illustrated in Fig. 2 – this shall serve as the control input.

Being a free endpoint problem, let the states of P and E be denoted by (x_p, x_e) . Furthermore, let the rockets be driven by their thrusts, denoted by (u_p, u_e) for P and E respectively (see Figure 2). We fix the range of the rockets so that what is left of the motion of either P or E 's is restricted to orientation on the (x, z) plane as illustrated in Fig. 2. Whence, the relevant kinematic equations (from equation (52)) are

$$\dot{x}_{2e} = x_{4e}; \quad \dot{x}_{2p} = x_{4p}, \quad (53a)$$

$$\dot{x}_{4e} = a \sin u_e - g; \quad \dot{x}_{4p} = a \sin u_p - g \quad (53b)$$

where a and g are respectively the acceleration and gravitational accelerations (in feet per square second)⁵.

We want to determine the outcome of a simulated game between the two agents over a time interval. In the process of this protracted simulation, the nature of the barrier surface of the target tube (henceforth called the backward reachable tube or BRT⁶) will change.

Our desideratum is determining if capture can be achieved at all in a “yes-or-no” fashion. Therefore, we pose the game over a finite range over outcomes so that the game at hand assumes Isaac’s [24] description of a *game of kind*. P can achieve as much proximity to a given *target set* as much as possible while E is set up to protect the *target set*. For example, one may take P as seeking to penetrate a (closed) territory (called *target*) under guard by player E ; and P ’s goal may be to maximize the time of play so as to penetrate the barrier surface of the target. E seeks to protect a given target’s surface. As long as E remains within this *backward reachable tube* (or BRT), P cannot cause damage or exercise an action of deleterious consequence on, say, the territory being guarded by E .

Setting up E to maximize the payoff quantity (55) with the largest possible margin or at least frustrate the efforts of P with minimal collateral damage while the pursuer minimizes the payoff quantity constitutes a terminal value *optimal* differential game: there is no optimal pursuit without an optimal evasion since P and E are both executing motions as they see fit within the problem parameters.

Therefore, we rewrite (52) with P ’s motion relative to E ’s along the (x, z) plane so that the relative orientation as shown in Fig. 2 is $\theta = u_p - u_e$ – this shall serve as the control input. Following the conventions in Fig. 2, the game’s relative equations of motion in *reduced space* [24, §2.2] i.e. is $\mathbf{x} = (x, z, \theta)$ where $\theta \in [-\frac{\pi}{2}, \frac{\pi}{2}]$ and $(x, z) \in \mathbb{R}^2$ are

$$\dot{\mathbf{x}} = \begin{cases} \dot{x} &= a_p \cos \theta + u_e x, \\ \dot{z} &= a_p \sin \theta + a_e + u_e x - g, \\ \dot{\theta} &= u_p - u_e. \end{cases} \quad (54)$$

The boundary of the *usable part* of the origin-centered circle of radius ϕ (we have set $\phi = 1.5$ feet in our evaluations) is $\|PE\|_2$ so that

$$\phi^2 = x^2 + z^2. \quad (55)$$

All capture points are specified by the variational HJ PDE [35]:

$$\frac{\partial \phi}{\partial t}(\mathbf{x}, t) + \min \left[0, H(\mathbf{x}, \frac{\partial \phi(\mathbf{x}, t)}{\partial \mathbf{x}}) \right] \leq 0, \quad (56)$$

with Hamiltonian given by

$$H(\mathbf{x}, p) = - \max_{u_e \in [\underline{u}_e, \bar{u}_e]} \min_{u_p \in [\underline{u}_p, \bar{u}_p]} \begin{bmatrix} p_1 & p_2 & p_3 \end{bmatrix} \begin{bmatrix} a_p \cos \theta + u_e x \\ a_p \sin \theta + a_e + u_p x - g \\ u_p - u_e \end{bmatrix} \quad (57)$$

Here, the co-states p is defined with a strict corresponding property, and $[\underline{u}_e, \bar{u}_e]$ denotes the extremals that the evader must choose as input in response to the extremal controls that the pursuer plays i.e. $[\underline{u}_p, \bar{u}_p]$.

We must consider the possibilities of behavior by either agent in an all-encompassing fashion in order to know what an outcome may be in the future should either agent execute different controls. Rather than resort to analytical *geometric reasoning*, we may analyze this *game* via a

⁵We set $a = 1ft/sec^2$ and $g = 32ft/sec^2$ in our simulation.

⁶It is called backward because the game is simulated backward in time.

principled numerical simulation. This is what we present next. From (57), set $\underline{u}_e = \underline{u}_p = \underline{u} \triangleq -1$ and $\bar{u}_p = \bar{u}_e = \bar{u} \triangleq +1$ so that

$$\begin{aligned}
 H(x, p) &= - \max_{u_e \in [\underline{u}_e, \bar{u}_e]} \min_{u_p \in [\underline{u}_p, \bar{u}_p]} \left[p_1(a_p \cos \theta + u_e x) + p_2(a_p \sin \theta + a_e + u_p x - g) + p_3(u_p - u_e) \right], \\
 &= -a_p p_1 \cos \theta - a_p p_2 \sin \theta - a_p p_2 + g p_2 - \max_{u_e \in [\underline{u}_e, \bar{u}_e]} \min_{u_p \in [\underline{u}_p, \bar{u}_p]} (p_1 u_e + p_2 u_p x + p_3(u_p - u_e)), \\
 &= -a_p p_1 \cos \theta - a_p p_2 \sin \theta - a_p p_2 + g p_2 - \bar{u} |p_1 x + p_3| + \underline{u} |p_2 x + p_3|, \\
 &\triangleq -a_p p_1 \cos \theta - p_2(g - a - a \sin \theta) - \bar{u} |p_1 x + p_3| + \underline{u} |p_2 x + p_3|,
 \end{aligned} \tag{58}$$

where the last line in (58) follows from setting $a_e = a_p \triangleq a$.

For the target set being guarded by E , we choose an implicit representation with a cylindrical mesh on a three-dimensional grid as our representation. The grid's nodes are uniformly spaced apart at a resolution of 100 points per dimension over the interval $[-64, 64]$. In numerically solving for the Hamiltonian (58), a TVD-RK discretization scheme [40] based on fluxes is used in choosing smooth nonoscillatory results as described in §6. Denote by (x, y, z) a generic point in \mathbb{R}^3 so that given mesh sizes $\Delta x, \Delta y, \Delta z, \Delta t > 0$, letters u, v, w represent functions on the x, y, z lattice: $\Delta = \{(x_i, y_j, z_k) : i, j, k \in \mathbb{Z}\}$. We define the numerical monotone flux $\hat{H}(x, p)$, of $H(x, p)$ as

$$\begin{aligned}
 \hat{H}(u^+, u^-, v^+, v^-, w^+, w^-) &= H\left(\frac{u^+ + u^-}{2}, \frac{v^+ + v^-}{2}, \frac{w^+ + w^-}{2}\right), \\
 &= -\frac{1}{2} \left[\alpha_x^{(i)_j} (u^+ - u^-) + \alpha_y^{(i)_j} (v^+ - v^-) + \alpha_z^{(i)_j} (w^+ - w^-) \right],
 \end{aligned} \tag{59}$$

where

$$\alpha_x = \max_{\substack{a \leq u \leq b \\ c \leq v \leq d \\ e \leq w \leq f}} |H_u(\cdot)|, \quad \alpha_y = \max_{\substack{a \leq u \leq b \\ c \leq v \leq d \\ e \leq w \leq f}} |H_v(\cdot)|, \quad \text{and} \quad \alpha_z = \max_{\substack{a \leq u \leq b \\ c \leq v \leq d \\ e \leq w \leq f}} |H_w(\cdot)| \tag{60}$$

are the dissipation coefficients, controlling the level of numerical viscosity in order to realize a stable solution that is physically realistic [10]. Here, the subscripts of H are the partial derivatives w.r.t the subscript variable, and the flux, $\hat{H}(\cdot)$ is monotone for $a \leq u^\pm \leq b, c \leq v^\pm \leq d, e \leq w^\pm \leq f$. It is easy to verify from (58) that

$$\alpha_x = |a \cos \theta| + |u|x|, \quad \alpha_y = |g - a - a \sin \theta| + |u|x|, \quad \text{and} \quad \alpha_z = |\bar{u}| + |\underline{u}|. \tag{61}$$

```

1 finite_diff_data = {"innerFunc": termLaxFriedrichs,
2 "innerData": {"grid": g, "hamFunc": rocket_rel.ham,
3 "partialFunc": rocket_rel.dissipation,
4 "dissFunc": artificialDissipationGLF,
5 "CoStateCalc": upwindFirstENO2},
6 "positive": True} // direction of approx. growth

```

Listing 4. HJ ENO2 computational scheme for the rockets.

The Hamiltonian, upwinding scheme, flux dissipation method, and the overapproximation parameter for the essentially non-oscillatory polynomial interpolatory data used in geometrically reasoning about the *target set* is set up as seen in Listing 4. The data structure `finite_diff_data` contains all the routines needed for adding dynamics to the original implicit surface representation of $v(x, t)$. The monotone spatial upwinding scheme used (here `termLaxFriedrichs` described in §5.5) is passed into the `innerFunc` query field. The explicit form of the Hamiltonian (see (58)) is passed to the `hamFunc` query field and the grid described in the foregoing is passed to the `grid` field. We adopted a second-order accurate upwinding scheme together with the `Lax-Friedrichs`

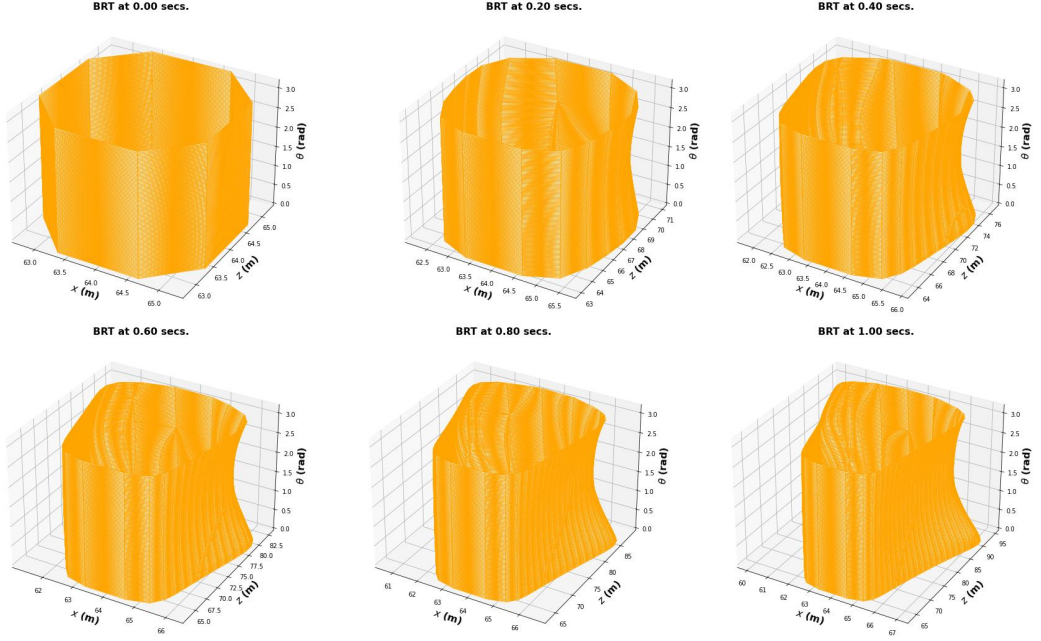


Fig. 3. (Left to Right): Backward reachable tubes (capture surfaces) for the rocket system (cf. Fig. 2) optimized for the paths of slowest-quickest descent in equation (57) at various time steps during the differential game. In all, the BRTs were computed using the method outlined in [8, 34, 37]. We set $a_e = a_p = 1ft/sec^2$ and $g = 32ft/sec^2$ as in Dreyfus' original example.

approximator. To indicate that we intend to overapproximate the value function, we specify a `True` parameter for the `positive` query field.

Safety is engendered by having the evader respond optimally to the pursuer at various times during the game. We are thus interested in the entire safety set over the time interval of play (i.e. the safety tube). The backward reachable tube (BRT) [35], under the control strategies of P or E , is a part of the phase space that constitutes $\Omega \times T$. We would like the BRT to cover as much of the entire phase space as possible. Thus, we *overapproximate* it. Using our GPU-accelerated levelset toolbox, we compute the *overapproximated* BRT of the game over a time span of $[-2.5, 0]$ seconds over 11 global optimization time steps. The BRTs at representative time steps in the optimization procedure is depicted in Fig. 3.

The initial value function (leftmost inset of Fig. 3) is represented as a (closed) dynamic implicit surface over all point sets in the state space (using a signed distance function) for a coordinate-aligned cylinder whose vertical axes runs parallel to the orientation of the rockets depicted in Fig. 2. This closed and bounded assumption of the target set is a prerequisite of the backward reachable analysis (see [35]). It allows us to include all limiting velocities. The two middle capture surfaces indicate the evolution of the capture surface (here the zero levelset) of the target set upon the optimal response of the evader to the pursuer. We reach convergence at the eleventh global optimization timestep (rightmost inset of Fig. 3).

Reachability theory thus affords us an ability to numerically reason about the behavior of these two rockets aforesaid in a principled manner. To do this, we have passed relevant parameters to the package as shown in Listing 4 and run a CFL constrained optimization scheme (as in Listing 3) for a finite number of global optimization timesteps. It is global because internally, there are other

local spatial and temporal finite differencing scheme that occurs “under the hood” (see 5 and the corresponding codes described).

7.2 Time Optimal Control: The Double Integral Plant

Here, we analyze a time-optimal control problem to determine what admissible control⁷ can “transport” the system under consideration to a desired “origin” in the shortest possible time. We consider the double integral plant [5, 44] as an illustrative example of our objective, which is to compute the points in the state space that can reach the origin in *finite-time* under the influence of a time-optimal controller.

We shall leverage standard necessary conditions from the principle of optimality [4] to obtain a time-optimal feedback control design; introduce the notion of isochrones and switching surfaces; and discuss the analytic and approximate solutions (with our library) to the time-optimal control problem for a double integrator. We shall conclude the section by comparing the analytic and the overapproximated numerical solution (using the LevelSetPy toolbox) to the time to reach the origin problem.

7.2.1 Dynamics and Problem Setup. The double integrator is controllable, so that open-loop strategies may be employed in driving specific states to the origin in finite time [44]. The plant has the following second-order dynamics

$$\ddot{\mathbf{x}}(t) = \mathbf{u}(t) \quad (62)$$

and admits bounded control signals $|\mathbf{u}(t)| \leq 1$ for all time t . After a change of variables, we have the following system of first-order differential equations

$$\begin{aligned} \dot{\mathbf{x}}_1(t) &= \mathbf{x}_2(t), \\ \dot{\mathbf{x}}_2(t) &= \mathbf{u}(t), \quad |\mathbf{u}(t)| \leq 1. \end{aligned} \quad (63)$$

The *reachability problem* that we consider is to address the question of what states can reach a certain point (here, the origin) in a transient manner. That is, we would like to find point sets on the state space, at a particular time step, such that we can bring the system to the equilibrium, $(0, 0)$.

7.2.2 Time-optimal control scheme. This is an H -minimal control problem whereupon we must find the control law that minimizes the Hamiltonian

$$H(\mathbf{x}, \mathbf{p}) = p_1 \dot{\mathbf{x}}_1 + p_2 \dot{\mathbf{x}}_2. \quad (64)$$

The necessary optimality condition stipulates that the minimizing control law be

$$\mathbf{u}(t) = -\text{sign}(p_2(t)) \triangleq \pm 1. \quad (65)$$

For the co-states in question, suppose that their initial values (for constants k_1 and k_2) are $p_1(t_0) = k_1$ and $p_2(t_0) = k_2$, only four candidates can serve as time-optimal control sequences i.e. $\{[+1], [-1], [+1, -1], [-1, +1]\}$. On a finite time interval, $t \in [t_0, t_f]$, the time-optimal $\mathbf{u}(t)$ is a constant $k \equiv \pm 1$ so that for initial conditions $\mathbf{x}_1(t_0) = \xi_1$ and $\mathbf{x}_2(t_0) = \xi_2$, it can be verified that the state trajectories obey the relation

$$\mathbf{x}_1(t) = \xi_1 + \frac{1}{2}k(\mathbf{x}_2^2 - \xi_2^2), \text{ for } t = k(\mathbf{x}_2(t) - \xi_2). \quad (66)$$

The trajectories of (66) traced out over a finite time horizon $t = [-1, 1]$ with *piecewise constant control laws*, $u = \pm 1$ on a state space and under the control laws $\mathbf{u}(t) = \pm 1$ is depicted in Fig. 4. Curves with arrows that point upwards denote trajectories under the control law $\mathbf{u} = +1$; call these

⁷A control law is admissible when its range belongs in the admissible input set where it is bounded.

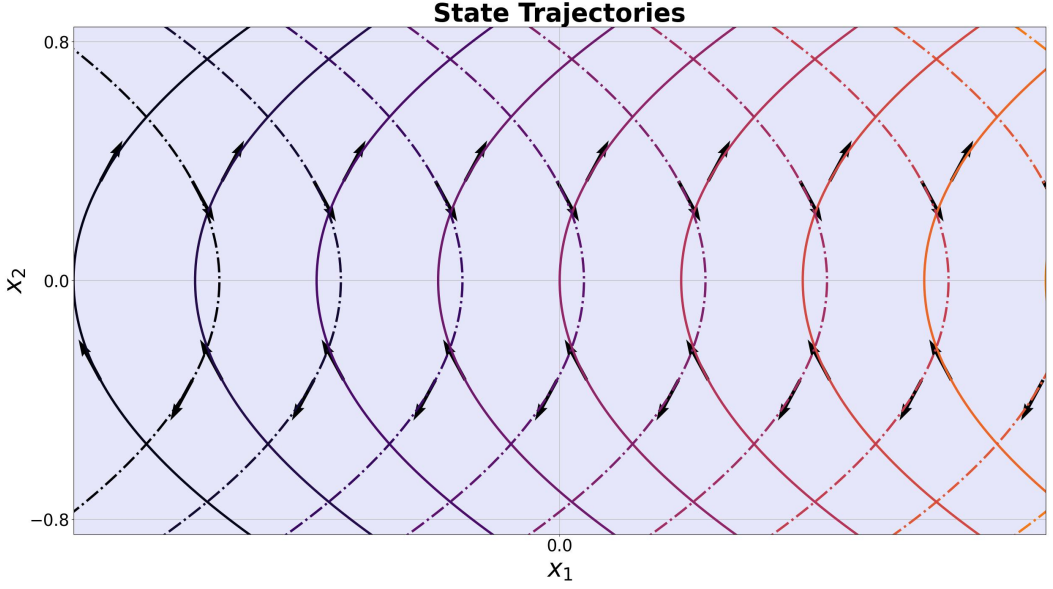


Fig. 4. State trajectories of the double integral plant. The solid curves are trajectories generated for $u = +1$ while the dashed curves are trajectories for $u = -1$.

trajectories γ_+ ; while the trajectories marked by dashed arrows pointing downward on the curves were executed under $u = -1$; call these trajectories γ_- .

7.2.3 Analytic Time to Reach the Origin. The *time to reach the origin* $(0, 0)$ from any other pair (x_1, x_2) on the state plane of Fig. 4 in the *shortest possible time* is our approximation problem. This minimum time admits an analytical solution given by [1]

$$t^*(x_1, x_2) = \begin{cases} x_2 + \sqrt{4x_1 + 2x_2^2} & \text{if } x_1 > \frac{1}{2}x_2|x_2| \\ -x_2 + \sqrt{-4x_1 + 2x_2^2} & \text{if } x_1 < -\frac{1}{2}x_2|x_2| \\ |x_2| & \text{if } x_1 = \frac{1}{2}x_2|x_2|. \end{cases} \quad (67)$$

The geometry (phase portrait) of (67) is shown in Fig. 5. Let us define γ_+ as the locus of all points (x_1, x_2) which can be forced to the origin by $u = +1$ i.e.

$$\gamma_+ = \{(x_1, x_2) : x_1 = \frac{1}{2}x_2^2; x_2 \leq 0\} \quad (68)$$

and let γ_- be the locus of all points (x_1, x_2) which can be forced to the origin by $u = -1$ i.e.

$$\gamma_- = \{(x_1, x_2) : x_1 = \frac{1}{2}x_2^2; x_2 \geq 0\}. \quad (69)$$

The confluence of the locus of points on γ_+ and γ_- is the *switching curve*, depicted in bright orange in Fig. 5, is

$$\gamma \triangleq \gamma_+ \cup \gamma_- = \left\{ (x_1, x_2) : x_1 = \frac{1}{2}x_2|x_2| \right\}. \quad (70)$$

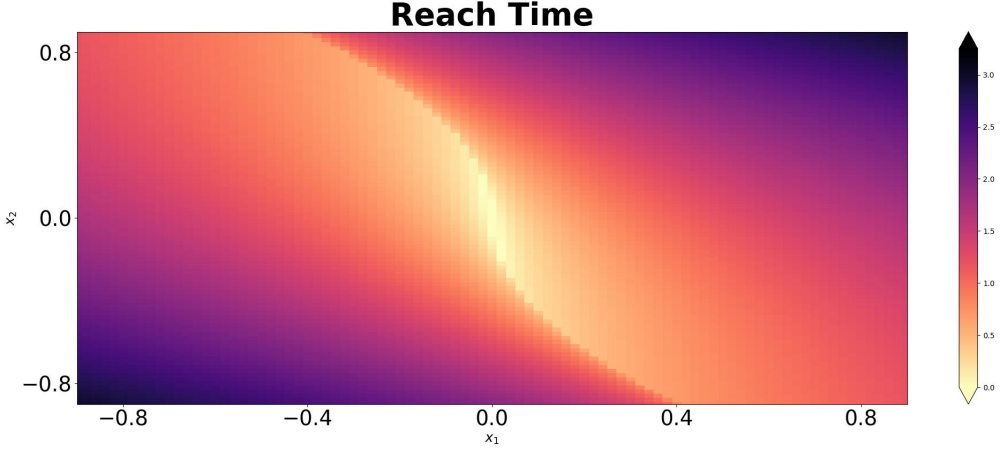


Fig. 5. Analytical time to reach the origin on the state grid, $(\mathbb{R} \times \mathbb{R})$; the switching curve, $\gamma = \gamma_- \cup \gamma_+$, passes through states on $(0, 0)$.

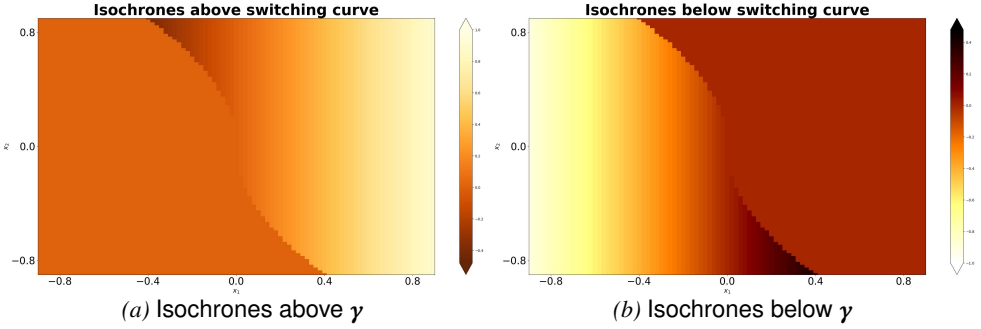


Fig. 6. (a) Isochrones for states above the switching curve, (b) states below the switching curve.

The *unique* time-optimal control law, \mathbf{u}^* , that solves this problem can be determined to be

$$\begin{aligned} \mathbf{u}^* &= \mathbf{u}^*(x_1, x_2) = +1 \quad \forall (x_1, x_2) \in \gamma_+ \cup \mathbb{R}_+, \\ \mathbf{u}^* &= \mathbf{u}^*(x_1, x_2) = -1 \quad \forall (x_1, x_2) \in \gamma_- \cup \mathbb{R}_-, \\ \mathbf{u}^* &= -\text{sgn}\{x_2\} \quad \forall (x_1, x_2) \in \gamma. \end{aligned} \quad (71)$$

The minimum cost for this problem is equivalent to the minimum time for states (x_1, x_2) to reach the origin $(0, 0)$. This is given as

$$\Phi^*(x, t) \triangleq t^*(x_1, x_2) \quad (72)$$

with the associated terminal value

$$-\frac{\partial \Phi^*(x, t)}{\partial t} = H\left(t, x, \frac{\partial \Phi^*(x, t)}{\partial t}, u\right) \Bigg|_{\substack{x=x^* \\ u=u^*}} \quad \text{with } H(t; x, u, p_1, p_2) = x_2(t)p_1(t) + u(t)p_2(t) \quad (73)$$

and

$$p_1 = \frac{\partial t^*}{\partial x_1}, \quad p_2 = \frac{\partial t^*}{\partial x_2}. \quad (74)$$

The HJ equation is given by

$$\begin{aligned}
 \frac{\partial \Phi^*}{\partial t} + x_2 \frac{\partial \Phi^*}{\partial x_1} - \frac{\partial \Phi^*}{\partial x_2} &= 0 & \text{if } x_1 > -\frac{1}{2}x_2|x_2|, \\
 \frac{\partial \Phi^*}{\partial t} + x_2 \frac{\partial \Phi^*}{\partial x_1} + \frac{\partial \Phi^*}{\partial x_2} &= 0 & \text{if } x_1 < -\frac{1}{2}x_2|x_2|, \\
 \frac{\partial \Phi^*}{\partial t} + x_2 \frac{\partial \Phi^*}{\partial x_1} - \text{sgn}\{x_2\} \frac{\partial \Phi^*}{\partial x_2} &= 0 & \text{if } x_1 = -\frac{1}{2}x_2|x_2|.
 \end{aligned} \tag{75}$$

The set of states (x_1, x_2) that can be forced to reach the origin in the same minimum time $t^* \equiv \Phi^*$ are the system's *isochrones* which are illustrated in Fig. 6. A point (x_1, x_2) on the state grid belongs to the set of states $S(t^*)$ from which it can be forced to the origin $(0, 0)$ in the same minimum time t^* . We call the set $S(t^*)$ the minimum isochrone. These are the isochrones of the system – akin to the isochrone map used in geography, hydrology, and transportation planning for depicting areas of equal travel time to a goal state. The level sets of (75) correspond to the *isochrones* of the system as illustrated in Fig. 6.

7.2.4 Approximate Time to Reach the Origin. We compare the analytical solution to the *time to reach (TTR) the origin* problem (see Fig. 6) against the approximated TTR solution using a dynamic implicit surface representation of the approximate value function. An ellipsoid with a radius of 1.0 along its major axis was chosen to represent the initial time to reach interface (see Fig. 7a, right inset). We then choose a controller with values ± 1 depending on which side of the switch surface Fig. 6 we are on in generating the system's phase portrait illustrated in Fig. 4.

The closed-form solution to the time-to-reach the origin problem on a 2-D grid with x/y axis limits $[[-1, 1], [-1, 1]]$ is shown in the left inset of Fig. 4a. We set out to investigate the result of adding dynamics (with levelsets) to the elliptic implicit representation of the analytical TTR and evaluate the efficacy of our computational scheme. We proceed as shown in Listing 6.

```

1 finite_diff_data = {"innerFunc": termLaxFriedrichs,
2   "innerData": {"grid": g, "hamFunc": dint.ham,
3   "partialFunc": dint.dissipation,
4   "dissFunc": artificialDissipationGLF,
5   "CoStateCalc": upwindFirstENO2},
6   "positive": False} // direction of approx. growth

```

Listing 5. Overapproximation setup for the double integrator TTR problem.

As a custom, a separate class (see `DoubleIntegrator` in the folder `DynamicalSystems`) holds all the dynamics (cref. equations 62 and 63), switching surface (cref. equations 68, 69, and 70), Hamiltonian (cref. equation 64), dissipation, and costates (cref. 74) of the double integrator plant. Over a twenty-step timespan ranging from 0 to 20, we integrate the right-hand-side of (75) forward in time by the Courant-Friedrichs-Lewy constrained second-order accurate integrator i.e. `odeCFL2` in our library:

```

1 t, y, ~ = odeCFL2(termRestrictUpdate, t_span, y0, options, finite_diff_data)

```

Listing 6. Overapproximation setup for the double integrator TTR problem.

where $y0$ is the initial elliptic function that represents Φ in (75), `options` are the set of integration parameters such as the number of actual timesteps to take in the adaptive integration scheme, the maximum step size and so on. The routine `termRestrictUpdate` restricts the sign of the update of the HJ approximation by either increasing or decreasing the levelset.

A side-by-side comparison of the level sets is shown in Fig. 7a. The approximation to the isochrones by our integration scheme is an overapproximation of the analytical TTR problem. This is illustrated in the right inset of Fig. 7a. Because we are not concerned with the safe set (unlike the example

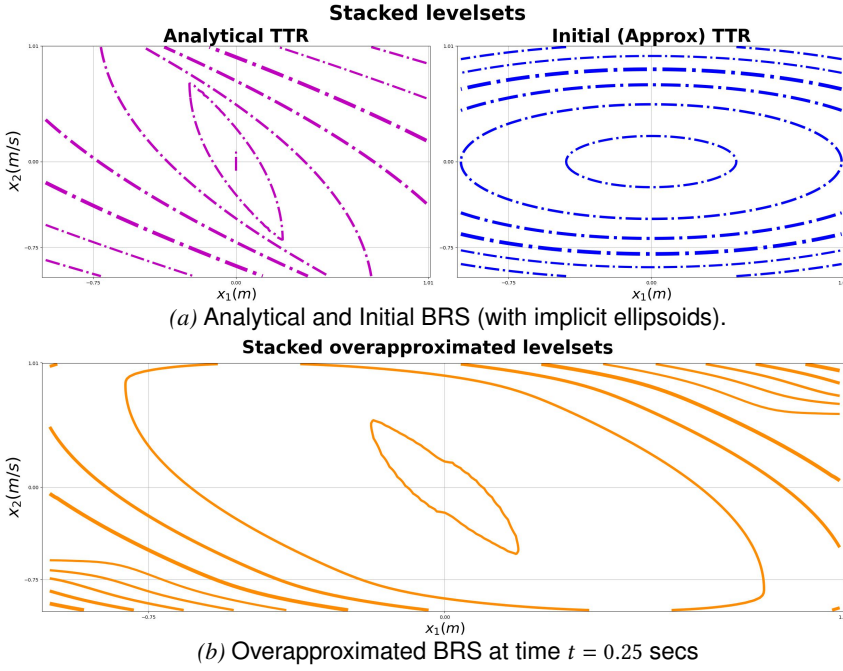


Fig. 7. Time to reach the origin at different integration time steps. Top-left: Closed-form Solution to the time to reach the origin problem. Top-right: Implicit representation of the initial TTR solution. Bottom: Lax-Friedrichs Approximation to the TTR the origin problem.

in 7.1), we do not overapproximate the time-to-reach solution. On the overall, we obtain similar isochrones to the analytical result, hence validating our hypothesis.

7.3 Reach-Avoid Games: Flocks within Starling Murmurations

Here, we will borrow inspiration from natural swarms, particularly the murmuration [19] of European starlings – the *sturnus vulgaris* – in our problem construction and solution concept. We are concerned with reach-avoid games in multiagent systems, whereupon agents must safely navigate a phase space (e.g. in achieving an attitude convergence goal), whilst avoiding collision with one another and capture by an external predator. A natural environment where this problem occurs is in the murmuration of European Starlings. In what follows, we formulate the problem mathematically and pose the collision avoidance for a local set of birds as a reachable differential game.

7.3.1 Problem Description. Consider a group of starlings moving on a space-time continuum $\Omega \times T^8$ as illustrated in Fig. 8. Recent field studies [7] suggest that emergent collective motion observed among these birds is as a result of local nearest neighbor interactions among separable subsets of bird groups on $\Omega \times T$. There is evidence with justifiable confidence [25] that suggests that when density varies among the birds (henceforth called agents), the relationship among birds in local groups is not determined by the metric distance among nearest neighbors but rather by a topological notion of distance (defined as the number of intermediate birds between one agent from another [2]). Starlings exhibit complex formation patterns that are effective in avoiding capture – mostly by peregrine Falcons in the wild [18].

⁸Here Ω is the open set that contains all states of the birds and T is the length of time over the real line.

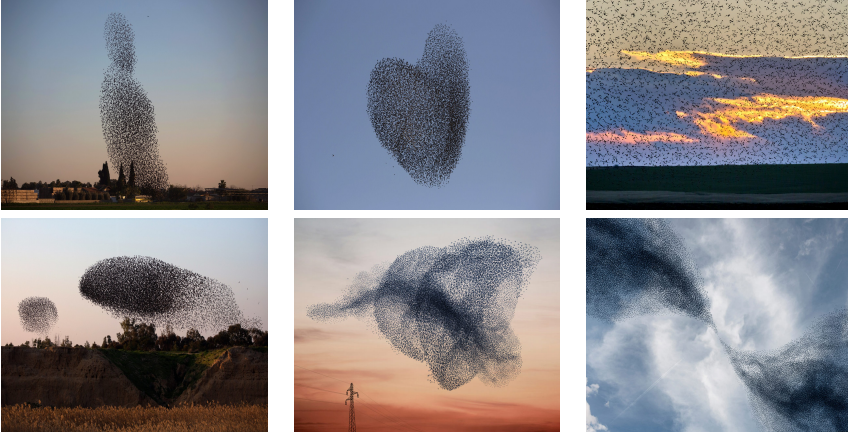


Fig. 8. Starlings murmurations. From the top-left and clockwise. (i) A starlings flock rises into the air, in a dense structure (Reuters/Amir Cohen). (ii) Starlings migrating over an Israeli village (AP Photo/Oded Balilty). (iii) Starlings feeding on laid seeds in the ground in Romania. (iv) Two flocks of migrating starlings (Menahem Kahana/AFP/Getty Images). (v) A concentric conical formation of starlings (Courtesy of The Gathering Site.). (vi) Splitting and joining of a flock of starlings.

We will leverage this notion of topological distance between agents in developing a target or safe set [22] for a subset of agents within the murmuration. If we can precompute this safe set, it can serve as e.g. a safety filter between a dynamical system consisting of multiagent systems (to be controlled) and their actual controller whilst respecting state constraints (e.g. topological distance between agents) and the control constraints (admissible inputs, dynamic update frequency of input control laws e.t.c.). We will defer the enumeration of the use of this safe set to a future publication seeing that paper is to prove the capability of the library that we have developed at succeeding at a host of multiple myriad complex problems.

7.3.2 Mathematical abstractions. Individual agents self-organize into phases or regions S which are in turn members of a union of multiple regions C . Note that every $S \subseteq C$ and all members of C are disjoint from one another i.e. $S_i \cup S_j = \emptyset$ for any $i \neq j$. The total number of elements in S is denoted $|S|$, and we denote by $\text{int } \Omega$ the interior of Ω . The closure of Ω is $\bar{\Omega}$. We let $\delta\Omega := \bar{\Omega} \setminus \text{int } \Omega$ be the boundary of Ω .

An evading agent in a region S_i has a state notation \mathbf{x}_a^i (read: the state of agent a in region i). A state \mathbf{x}_a^i has linear velocity components, $\mathbf{x}_{a_1}^i, \mathbf{x}_{a_2}^i$, and heading $\mathbf{x}_{a_3}^i := \mathbf{w}_a^i$. When we must distinguish an agent $\mathbf{x}_a^i \in C_x$ from some other agent e.g. in another multiphase C_y , we shall write $^x\mathbf{x}_a^i$ and $^y\mathbf{x}_a^i$ respectively.

The set of players in a game is denoted $\mathcal{N} = \{i, j, \dots\}$ with subscript indexing indicating players e.g. N_i for player i . The set of neighbors of player i is $\mathcal{N}(i) \subseteq \mathcal{N}$. Player i moves dynamically with a control $u_i \in \pi_i$ (i.e. u_i belongs to a policy class π_i) that is both (a) optimal with respect to its own objective \mathcal{J}_i ; and (b) optimal with respect to its neighboring players' current policy $\pi_{-i} \in \Pi_{j \in \mathcal{N}, j \neq i}$. Neighbors of agent i at time t are those which are either within, or on a circle specified by a fixed topological range, r_c . This topological range is given by the difference in the numerical label of individuals (see Definition 2), and is consistent with findings in collective swarm behaviors as it reinforces *group cohesion* [2].

The topological metric is given by the label of an agent and it quantifies the number of intermediate agents that separate two agents. This is consistent with collective animal behaviors where individuals'

bookkeeping on their neighbors' positions help maintain the strength of an interaction when density varies or when they need to reorient a control input, given by the average of its own orientation and that of its neighbors. Instead of metric distance interaction rules that make agents very vulnerable to predation [2], we resort to a topological interaction rule⁹.

DEFINITION 2. *We define a flock, F , consisting of agents labeled $\{1, 2, \dots, n_a\}$ as a collection of agents within a phase space $(\Omega \times T)$ such that all agents within the flock interact with their nearest neighbors in a topological sense.*

ASSUMPTION 1. *Every agent within a flock has similar dynamics to that of its neighbor(s). Furthermore, agents travel at the same linear speed, v ; the angular headings, w , however, may be different between agents, seeing we are dealing with a many-bodied system. Each agent's continuous-time dynamics, $\dot{\mathbf{x}}^{(i)}(t)$, evolves as*

$$\begin{bmatrix} \dot{\mathbf{x}}_1^{(i)}(t) \\ \dot{\mathbf{x}}_2^{(i)}(t) \\ \dot{\mathbf{x}}_3^{(i)}(t) \end{bmatrix} = \begin{bmatrix} v(t) \cos \mathbf{x}_3^{(i)}(t) \\ v(t) \sin \mathbf{x}_3^{(i)}(t) \\ \langle \mathbf{w}^{(i)}(t) \rangle_r \end{bmatrix}, \langle \mathbf{w}^{(i)}(t) \rangle_r = \frac{1}{1 + n_i(t)} \left(\mathbf{w}^{(i)}(t) + \sum_{j \in \mathcal{N}_i(t)} \mathbf{w}_j(t) \right) \quad (76)$$

for agents $i = \{1, 2, 3, \dots, n_a\}$, where t is the continuous-time index, $n_i(t)$ is the number of agent i 's neighbors at time t , $\mathcal{N}_i(t)$ denotes the sets of labels of agent i 's neighbors at time t , and $\langle \mathbf{w}^{(i)}(t) \rangle_r$ is the average orientation of agent i and its neighbors at time t .

REMARK 1. *Note that for a game where all agents share the same constant linear speed and heading, (77) reduces to the dynamics of a Dubins' vehicle in absolute coordinates with $-\pi \leq \mathbf{w}^{(i)}(t) < \pi$. The averaging over the degrees of freedom of other agents in (77) is consistent with mean field theory, whereby the effect of all other agents on any one agent is an approximation of a single averaged influence.*

7.3.3 Agents' Motion as Differential Games. Structural homogeneity of agents' motion in every region $S_i \in \mathcal{C}$ for $i = 1, \dots, [C]$ applies. In starlings dynamic behavior, the flying performance is often spurred by a predator. In our formulation, this is enforced by introducing an external disturbance on the zeroth-index agent within a local region (this aids compactness of the zero levelset of an S_i as the theory of HJ Reachability recommends [35]). However, we are interested in *robust group cohesion* in reachability analysis. Therefore, we let a pursuer, P , with a worst-possible disturbance attack the flock, and we take it that flocks of agents constitute an evading player, E .

We must find a mathematical way to replicate the collision-avoidance scheme that these birds execute in the real-world. Therefore, we locally synthesize the kinematics of agents in a manner amenable to state representation by resolving local payoff extremals, $\{\phi_1, \dots, \phi_{n_f}\}$. This is a state space partition induced by an aggregation of desired collective behavior from local flocks' values $\{v_1, \dots, v_{n_f}\}$ ¹⁰.

Suppose that the local control laws are properly coordinated, the region of the state space across which their coordinated influence might be exerted constitute a larger e.g. *manipulability volume* for a dexterous kinematic task. We now formalize definitions that will aid the modularization of the problem into manageable forms.

⁹With metric distance rules, we will have to formulate the breaking apart of value functions that encode a consensus heading problem in order to resolve the extrema of multiple payoffs; which is typically what we want to mitigate against during real-world autonomous tasks.

¹⁰Let the cursory reader understand that we use the concept of a flock loosely. The value function could represent a palette of composed value functions whose extremals resolve local behaviors we would like to emerge over separated local regions of the state space of dexterous drone acrobatics [27], a robot balls juggling task [6], or any parallel task domain verification problem.

DEFINITION 3 (PAYOFF OF A FLOCK). To every flock F_j (with a finite number of agents n_a) within a murmuration, $j = \{1, 2, \dots, n_f\}$, we associate a payoff, Φ_j , that is the union of all respective agent's payoffs for expressing the outcome of a desired kinematic behavior.

REMARK 2. Every agent within a flock has similar dynamics to that of its neighbor(s). Furthermore, agents travel at the same linear speed, v ; the angular headings, w , however, may be different between agents, seeing we are dealing with a many-bodied system. Each agent's continuous-time dynamics, $\dot{\mathbf{x}}^{(i)}(t)$, evolves as

$$\begin{bmatrix} \dot{\mathbf{x}}_1^{(i)}(t) \\ \dot{\mathbf{x}}_2^{(i)}(t) \\ \dot{\mathbf{x}}_3^{(i)}(t) \end{bmatrix} = \begin{bmatrix} v(t) \cos \mathbf{x}_3^{(i)}(t) \\ v(t) \sin \mathbf{x}_3^{(i)}(t) \\ \langle \mathbf{w}^{(i)}(t) \rangle_r \end{bmatrix}, \langle \mathbf{w}^{(i)}(t) \rangle_r = \frac{1}{1 + n_i(t)} \left(\mathbf{w}^{(i)}(t) + \sum_{j \in N_i(t)} \mathbf{w}_j(t) \right) \quad (77)$$

for agents $i = \{1, 2, 3, \dots, n_a\}$, where t is the continuous-time index, $n_i(t)$ is the number of agent i 's neighbors at time t , $N_i(t)$ denotes the sets of labels of agent i 's neighbors at time t , and $\langle \mathbf{w}^{(i)}(t) \rangle_r$ is the average orientation of agent i and its neighbors at time t . Note that for a game where all agents share the same constant linear speed and heading, (77) reduces to the dynamics of a Dubins' vehicle in absolute coordinates with $-\pi \leq \mathbf{w}^{(i)}(t) < \pi$. The averaging over the degrees of freedom of other agents in (77) is consistent with the mean field theory, whereby the effect of all other agents on any one agent is an approximation of a single averaged influence.

7.3.4 Framework for Separated Payoffs. Suppose that a murmuration's global heading is given and that each agent i within each flock, F_j , ($j = \{1, \dots, n_f\}$) in the murmuration has a constant linear velocity, v^i . An agent's orientation is its control input, given by the average of its own orientation and that of its neighbors. What constitutes an agent's neighbors are computed based on empirical findings and studies from the lateral vision of birds and fishes [2, 21, 25] that provide insights into their anisotropic kinematic density and structure. Importantly, starlings' lateral visual axes and their lack of a rear sector reinforces their lack of nearest neighbors in the front-rear direction. As such, this enables them to maintain a tight density and robust heading during formation and flight.

The delineation of an agent's nearest neighbors is given in Algorithm 1. On lines 3 and 7 of Algorithm 1, cohesion is reinforced by leveraging the observations above. While the neighbor updates for an agent involve an $O(n^2)$ algorithm in Algorithm 1, we are merely dealing with 6 – 7 agents at a time in a local flock – making the computational cost measly.

Each agent within a flock F_j interacts with a fixed number of neighbors, n_c , within a fixed topological range, r_c . The topological range can be set as the distance between the labels of agents in a flock. This topological range is consistent with findings in collective swarm behaviors and it reinforces *group cohesion* [2]. However, we are interested in *robust group cohesion* in reachability analysis. Therefore, we let a pursuer, P , with a worst-possible disturbance attack the flock, and we take it that flocks of agents constitute an evading player, E .

7.3.5 Global Isotropy via Local Anisotropy. Structural anisotropy is not merely an effect of a preferential velocity in animal flocking kinematics but rather an explicit effect of the anisotropic interaction character itself: agents choose a mutual position on the state space in order to maximize the sensitivity to changes in heading and speed of neighbors as the neighbors' anisotropy is optimized via vision-based collision avoidance characteristically unrelated to the eye's structure [2].

To reinforce robust group cohesion in local flocks, we randomly simulate a pursuer P_j against an evading agent in every flock F_j so that one agent is always in relative coordinates with P^j . In this specialized case, E and P 's speeds and maximum turn radii are equal: if both players start the game with the same initial velocity and orientation, the relative equations of motion show that E can mimic P 's strategy by forever keeping the starting radial separation. As such, the *barrier* is closed

Algorithm 1 Nearest Neighbors For Agents in a Flock.

```

1: Given a set of agents  $\mathbf{a} = \{a_1, a_2, \dots, a_{n_a} \mid [a] = n_a\}$  ▷  $n_a$  agents in a flock  $F_k$ .
2: function UpdateNeighbor( $n$ )
3:   for  $i$  in  $1, \dots, n$  do ▷ Look to the right and update neighbors.
4:     for  $j$  in  $i + 1, \dots, n$  do
5:       COMPARE_NEIGHBOR( $a[i], a[j]$ )
6:     end for
7:     for  $j$  in  $i - 1$  down to  $0$  do ▷ Look to the left and update neighbors.
8:       COMPARE_NEIGHBOR( $a[i], a[j]$ )
9:     end for
10:  end for
11:  for each  $a_i \in F_k, i = 1, \dots, n_a$  do ▷ Recursively update agents' headings.
12:    Update headings according to (77).
13:  end for
14: end function


---


1: function Compare_Neighbor( $a_1, a_2$ ) ▷ ( $a_1, a_2$ ): distinct instances of AGENT.
2:   if  $|a_1.\text{label} - a_2.\text{label}| < a_1.r_c^1$  ▷  $r_c^n$ : agent  $n$ 's capture radius,  $r_c$ .
3:      $a_1.\text{UPDATE\_NEIGHBORS}(a_2)$  then
4:   end if
5: end function


---


1: procedure Agent( $a_i, \text{Neighbors}=\{\}$ ) ▷ Neighbors: Set of neighbors of this agent.
2:   ▷ Agent  $a_i$  with attributes  $\text{label} \in \mathbb{N}$ , avoid and capture radii,  $r_a, r_c$ .
3:   function UPDATE_NEIGHBORS(neigh)
4:     if  $\text{length}(\text{neigh}) > 1$  then ▷ Multiple neighbors.
5:       for each neighbor of neigh do
6:         UPDATE_NEIGHBORS(neighbor) ▷ Recursive updates.
7:       end for
8:     end if
9:     Add neigh to Neighbors
10:  end function
11: end procedure

```

and the central theme in this game of kind is to determine the surface of the boundary [31]. We defer a thorough analysis of the nature of the surface to a future work.

Owing to the high-dimensionality of the state space, we cannot resolve this barrier analytically, hence we resort to numerical approximation methods – in particular, we leverage a parallel Lax-Friedrichs integration scheme [8] which we implement in Cupy [36] in order to provide a *consistent* and *monotone* solution to the Hamiltonians of the flocks. The assembly in the large of these respective Hamiltonians, and hence numerically robust solutions to the variational backward reachability problem is resolved with a Voronoi tessellation of the zero-level sets of the boundaries of the flocks.

Therefore, for an agent i within a flock with index j in a murmuration, the equations of motion under attack from a predator p in relative coordinates is

$$\begin{bmatrix} \dot{\mathbf{x}}_1^{(i)j}(t) \\ \dot{\mathbf{x}}_2^{(i)j}(t) \\ \dot{\mathbf{x}}_3^{(i)j}(t) \end{bmatrix} = \begin{bmatrix} -v_e^{(i)j}(t) + v_p^{(j)} \cos \mathbf{x}_3^{(i)j}(t) + \langle \mathbf{w}_e^{(i)j} \rangle_r \mathbf{x}_2^{(i)j}(t) \\ v_p^{(i)j}(t) \sin \mathbf{x}_3^{(i)j}(t) - \langle \mathbf{w}_e^{(i)j} \rangle_r \mathbf{x}_1^{(i)j}(t) \\ \mathbf{w}_p^{(j)}(t) - \langle \mathbf{w}_e^{(i)j} \rangle_r \end{bmatrix} \quad \text{for } i = 1, \dots, n_a \quad (78)$$

where n_a is the number of agents within a flock, $(\mathbf{x}_1^{(i)j}(t), \mathbf{x}_2^{(i)j}(t)) \in \mathbb{R}^2$, and we have $\mathbf{x}_3^{(i)j}(t) \in [-\pi, +\pi]$ ¹¹. Read $\mathbf{x}_1^{(i)j}(t)$: the first component of the state of an agent i at time t which belongs to the flock j in the murmuration at time t . In absolute coordinates, the equation of motion for *free agents* is

$$\begin{bmatrix} \dot{\mathbf{x}}_1^{(i)j}(t) \\ \dot{\mathbf{x}}_2^{(i)j}(t) \\ \dot{\mathbf{x}}_3^{(i)j}(t) \end{bmatrix} = \begin{bmatrix} v_e^{(i)j}(t) \cos \mathbf{x}_3^{(i)j}(t) \\ v_e^{(i)j}(t) \sin \mathbf{x}_3^{(i)j}(t) \\ \langle \mathbf{w}_e^{(i)j}(t) \rangle_r \end{bmatrix}. \quad (79)$$

7.3.6 Flock Motion from Aggregated Value Functions. We introduce the union operator i.e. \cup below as an aggregation symbol since the respective payoffs of each agent in a flock may be implicitly or explicitly constructed¹² – when it is implicitly represented, say from a signed distance function, we shall aggregate the payoff of agents 1 and 2 as

$$\cup \{\phi_1(\mathbf{x}, t), \phi_2(\mathbf{x}, t)\} \equiv \phi_1(\mathbf{x}, t) \cup \phi_2(\mathbf{x}, t) = \min(\phi_1(\mathbf{x}, t), \phi_2(\mathbf{x}, t)) \quad (80)$$

otherwise, other appropriate arithmetic or logical operation shall apply.

We assume that the *value* of a flock heading control (differential game) exists. And by an extension of Hamilton's principle of least action, the terminal motion of a flock coincide with the extremal of the payoff functional

$$v(\mathbf{x}, t) = \inf_{\beta^{(1)} \in \mathcal{B}^{(1)}} \sup_{\mathbf{u}^{(1)} \in \mathcal{U}^{(1)}} \left[g^{(1)}(\mathbf{x}(T)) \right] \cup \dots \inf_{\beta^{(n_f)} \in \mathcal{B}^{(n_f)}} \sup_{\mathbf{u}^{(n_f)} \in \mathcal{U}^{(n_f)}} \left[g^{(n_f)}(\mathbf{x}(T)) \right]$$

where n_f is the total number of distinct flocks in a murmuration. The resolution of this equation admits a viscosity solution to the following variational terminal HJI PDE [35]

$$\bigcup_{j=1}^{n_f} \left[\bigcup_{i=1}^{n_a} \left(\frac{\partial v_i}{\partial t}(\mathbf{x}, t) + \min \left[0, H^{(i)}(\mathbf{x}^{(i)}, \mathbf{v}_x(\mathbf{x}, t)) \right] \right) \right] = 0. \quad (81)$$

with Hamiltonian,

$$H^{(i)}(t; \mathbf{x}^{(i)}, \mathbf{u}^{(i)}, \mathbf{v}^{(i)}, p^{(i)}) = \max_{\mathbf{u}^{(i)} \in \mathcal{U}^{(i)}} \min_{\mathbf{v}^{(i)} \in \mathcal{V}^{(i)}} \langle f^{(i)}(t; \mathbf{x}, \mathbf{u}^{(i)}, \mathbf{v}^{(i)}), p^{(i)} \rangle. \quad (82)$$

In swarms' collective motion, when e.g. a Peregrine Falcon attacks, immediate nearest agents change direction almost instantaneously. And because of the interdependence of the orientations of individual agents with respect to one another, all other agents respond instantaneously. Thus, we only simulate a single attack against a flock within the murmuration to realize robust cohesion.

A pursuer can attack any flock within the murmuration from a distinct surface: a P direction: this side of the surface reached after penetration in the $P - [E]$ -direction is the $P - [E]$ *side*[24]. We attribute the term *in the small* to determine the smooth parts of the singular surface solution when a pursuer attacks, and when they are stitched together into the total solution, we shall describe them as *in the large*. There exists at least one value $\bar{\alpha}$ of α such that if $\alpha = \bar{\alpha}$, no vector in the β -vctogram¹³ penetrates the surface in the E -direction. Similar arguments can be made for $\bar{\beta}$ which prevents penetration in the P -direction. We adopt [24]'s terminology and call these surfaces semi-permeable surfaces (SPS).

Throughout the game, we assume that the roles of P and E do not change, so that when capture can occur, a necessary condition to be satisfied by the saddle-point controls of the players is the Hamiltonian, $H^i(\mathbf{x}, p)$.

¹¹We have multiplied the dynamics by -1 so that the extremal's resolution evolves backwards in time.

¹²In resolving the zero-level sets of HJ value functions, it is typical to represent the payoff's surface as the isocontour of some function (usually a signed distance function).

¹³A β -vctogram is the resulting state space when a the strategy β is applied in computing the optimal control law for an agent.

THEOREM 1. *For a flock, F_j , the Hamiltonian is the total energy given by a summation of the exerted energy by each agent i so that we can write the main equation or total Hamiltonian of a murmuration as*

$$H(\mathbf{x}, p) = \max_{\mathbf{w}_e^{(k)j} \in [\underline{\mathbf{w}}_e^j, \bar{\mathbf{w}}_e^j]} \min_{\mathbf{w}_p^{(k)j} \in [\underline{\mathbf{w}}_p^j, \bar{\mathbf{w}}_p^j]} \bigcup_{j=1}^{n_f} \left[H_a^{(k)j}(\mathbf{x}, p) \cup \left(\bigcup_{i=1}^{n_a-1} H_f^{(i)j}(\mathbf{x}, p) \right) \right] \quad (83)$$

$$\begin{aligned} &\triangleq \bigcup_{j=1}^{n_f} \left(\bigcup_{i=1}^{n_a-1} \left[p_1^{(i)j} v^{(i)j} \cos \mathbf{x}_3 + p_2^{(i)j} v^{(i)j} \sin \mathbf{x}_3 + p_3^{(i)j} \langle \mathbf{w}_e^{(i)j} \rangle_r \right] \right. \\ &\quad \cup \left[p_1^{(k)j} \left(v^{(k)j} - v^{(k)j} \cos \mathbf{x}_3^{(k)j} \right) - p_2^{(k)j} v^{(k)j} \sin \mathbf{x}_3^{(k)j} - \underline{\mathbf{w}}_p^j |p_3^{(k)j}| \right. \\ &\quad \left. \left. + \bar{\mathbf{w}}_e^j \left[p_2^{(k)j} \mathbf{x}_1^{(k)j} - p_1^{(k)j} \mathbf{x}_2^{(k)j} + p_3^{(k)j} \right] \right] \right). \end{aligned} \quad (84)$$

where $H_a^{(k)j}(\mathbf{x}, p)$ is the Hamiltonian of the individual under attack by a pursuing agent, P , and $H_f^{(i)j}(\mathbf{x}, p)$ are the respective Hamiltonians of the free agents, $i = \{1, \dots, n_f\}$, within an evading flock in a murmuration, and not under the direct influence of capture or attack by P ; we denote by $\mathbf{w}_e^{(i)j}$ the heading of an evader i within a flock j and $\mathbf{w}_p^{(j)}$ the heading of a pursuer aimed at flock j ; $\underline{\mathbf{w}}_e^{(k)j}$ is the orientation that corresponds to the orientation of the agent with minimum turn radius among all the neighbors of agent k , inclusive of agent k at time t ; similarly, $\bar{\mathbf{w}}_e^{(k)j}$ is the maximum orientation among all of the orientation of agent k 's neighbors.

PROOF OF THEOREM 1. We write the Hamiltonian of the free agents in absolute coordinates and the Hamiltonian of the agent under attack in relative coordinates with respect to the pursuer. A flock's Hamiltonian is Hamiltonian of the free agents is the aggregation of all the mechanical energy in the system in absolute coordinates i.e.

$$\bigcup_{i=1}^{n_a-1} H_f^{(i)j}(\mathbf{x}, p) = \bigcup_{i=1}^{n_a-1} \begin{bmatrix} p_1^{(i)j} & p_3^{(i)j} & p_3^{(i)j} \end{bmatrix} \begin{bmatrix} v^{(i)j} \cos \mathbf{x}_3 \\ v^{(i)j} \sin \mathbf{x}_3 \\ \langle \mathbf{w}_e^{(i)j} \rangle_r \end{bmatrix} \quad (85)$$

where we have again dropped the time arguments for convenience. It follows that

$$\bigcup_{i=1}^{n_a-1} H_f^{(i)j}(\mathbf{x}, p) = \bigcup_{i=1}^{n_a-1} \left[p_1^{(i)j} v^{(i)j} \cos \mathbf{x}_3 + p_3^{(i)j} v^{(i)j} \sin \mathbf{x}_3 + p_3^{(i)j} \langle \mathbf{w}_e^{(i)j} \rangle_r \right]. \quad (86)$$

Equation (84) can be re-written as

$$H_a^{(k)j}(\mathbf{x}, p) = - \left(\max_{\mathbf{w}_e^{(k)j} \in [\underline{\mathbf{w}}_e^j, \bar{\mathbf{w}}_e^j]} \min_{\mathbf{w}_p^{(k)j} \in [\underline{\mathbf{w}}_p^j, \bar{\mathbf{w}}_p^j]} \begin{bmatrix} p_1^{(k)j}(t) & p_2^{(k)j}(t) & p_3^{(k)j}(t) \end{bmatrix} \begin{bmatrix} -v_e^{(k)j}(t) + v_p^{(j)} \cos \mathbf{x}_3^{(k)j}(t) + \langle \mathbf{w}_e^{(k)j} \rangle_r(t) \mathbf{x}_2^{(k)j}(t) \\ v_p^j(t) \sin \mathbf{x}_3^{(k)j}(t) - \langle \mathbf{w}_e^{(k)j} \rangle_r(t) \mathbf{x}_1^{(k)j}(t) \\ \mathbf{w}_p^j(t) - \langle \mathbf{w}_e^{(k)j} \rangle_r(t) \end{bmatrix} \right), \quad (87)$$

where $p_l^{(k)j}(t) \mid_{l=1,2,3}$ are the adjoint vectors [31]. For the pursuer, its minimum and maximum turn rates are fixed so that we have $\underline{\mathbf{w}}_p^j$ as the minimum turn bound of the pursuing vehicle, and $\bar{\mathbf{w}}_p^j$ is the maximum turn bound of the pursuing vehicle. Henceforth, we drop the templated time arguments for

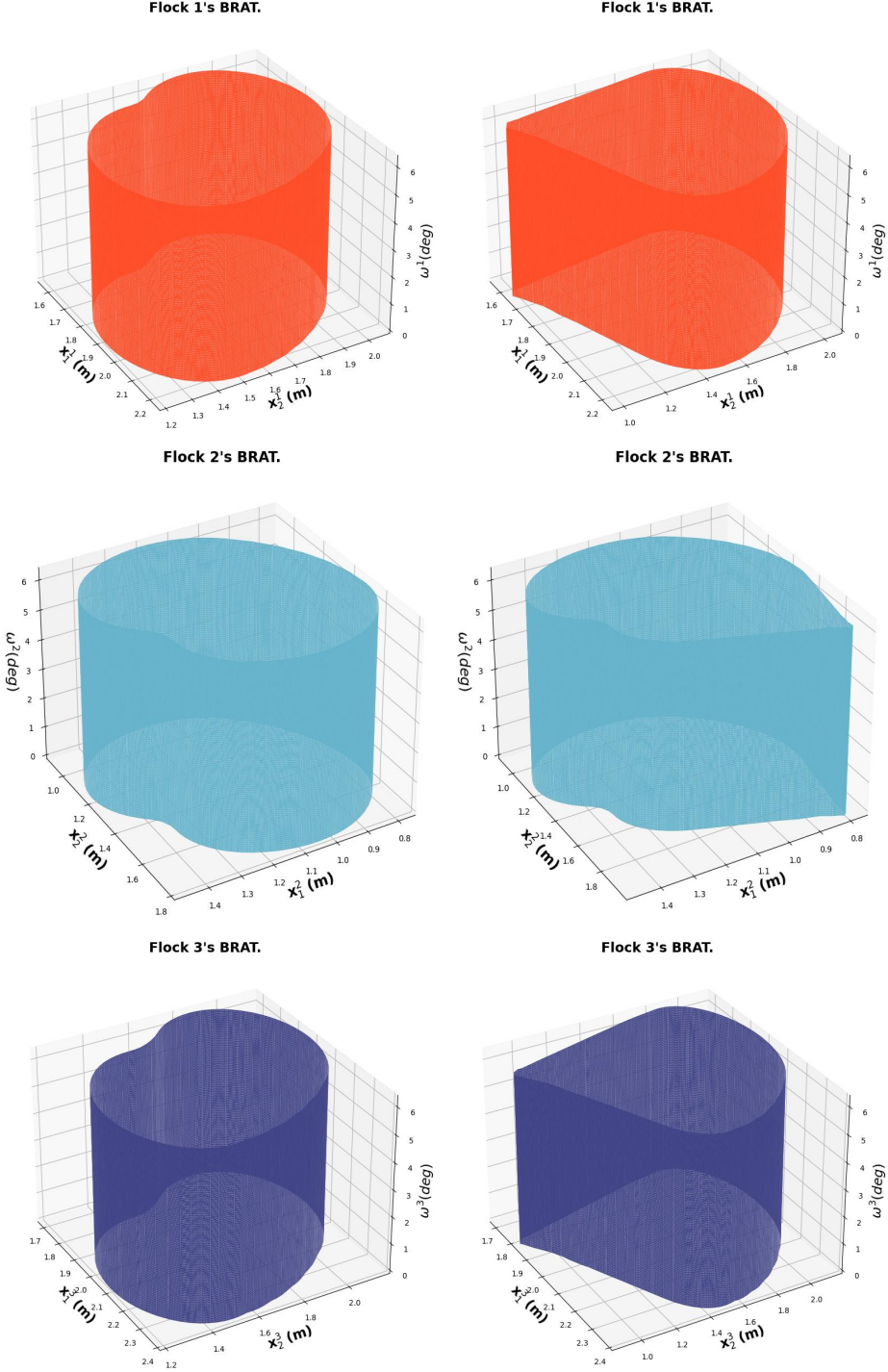


Fig. 9. Left column: Initial zero-level set for various flocks at different initial conditions. Right column: Evading flock's interface under a pursuer's attack after specific Lax-Friedrichs' integration. (Metric reach radius= $0.2m$, Avoid Radius= $0.2m$).

ease of readability. Rewriting (87), we find that

$$\begin{aligned}
 H_a^{(k)_j}(\mathbf{x}, p) = & - \left(\max_{\mathbf{w}_e^{(k)_j} \in [\underline{\mathbf{w}}_e^j, \tilde{\mathbf{w}}_e^j]} \min_{\mathbf{w}_p^{(k)_j} \in [\underline{\mathbf{w}}_p^j, \tilde{\mathbf{w}}_p^j]} \left[-p_1^{(k)_j} v_e^{(k)_j} + p_1^{(k)_j} v_p^j \cos \mathbf{x}_3^{(k)_j} \right. \right. \\
 & + p_1^{(k)_j} \langle \mathbf{w}_e^{(k)_j} \rangle_r \mathbf{x}_2^{(k)_j} + p_2^{(k)_j} v_p^j \sin \mathbf{x}_3^{(k)_j} - p_2^{(k)_j} \langle \mathbf{w}_e^{(k)_j} \rangle_r \mathbf{x}_1^{(i)_j} + p_3^{(k)_j} \left(\mathbf{w}_p^j - \langle \mathbf{w}_e^{(k)_j} \rangle_r \right) \Big] \Bigg), \\
 = & p_1^{(k)_j} \left(v_e^{(k)_j} - v_p^j \cos \mathbf{x}_3^{(k)_j} \right) - p_2^{(k)_j} v_p^j \sin \mathbf{x}_3^{(k)_j} \\
 & + \left(\max_{\langle \mathbf{w}_e^{(k)_j} \rangle_r \in [\underline{\mathbf{w}}_e^j, \tilde{\mathbf{w}}_e^j]} \min_{\mathbf{w}_p^j \in [\underline{\mathbf{w}}_p^j, \tilde{\mathbf{w}}_p^j]} \left[\langle \mathbf{w}_e^{(k)_j} \rangle_r \left(p_2^{(k)_j} \mathbf{x}_1^{(k)_j} - p_1^{(k)_j} \mathbf{x}_2^{(k)_j} + p_3^{(k)_j} \right) - p_3^{(k)_j} \mathbf{w}_p^j \right] \right).
 \end{aligned} \tag{88}$$

It follows that we have from (88) that

$$\begin{aligned}
 H_a^{(k)_j}(\mathbf{x}, p) = & p_1^{(k)_j} \left(v_e^{(k)_j} - v_p^j \cos \mathbf{x}_3^{(k)_j} \right) - p_2^{(k)_j} v_p^j \sin \mathbf{x}_3^{(k)_j} - \underline{\mathbf{w}}_p^j |p_3^{(k)_j}| \\
 & + \tilde{\mathbf{w}}_e^j \left| p_2^{(k)_j} \mathbf{x}_1^{(k)_j} - p_1^{(k)_j} \mathbf{x}_2^{(k)_j} + p_3^{(k)_j} \right|
 \end{aligned} \tag{89}$$

and that

$$H_f^{(i)_j}(\mathbf{x}, p) = \left[p_1^{(i)_j} v^{(i)_j} \cos \mathbf{x}_3 + p_2^{(i)_j} v^{(i)_j} \sin \mathbf{x}_3 + p_3^{(i)_j} \langle \mathbf{w}_e^{(i)_j} \rangle_r \right]. \tag{90}$$

A fortiori the main equation (84) becomes

$$\begin{aligned}
 H(\mathbf{x}, p) = & \cup_{j=1}^{n_f} \left(\cup_{i=1}^{n_a-1} \left[p_1^{(i)_j} v^{(i)_j} \cos \mathbf{x}_3 + p_2^{(i)_j} v^{(i)_j} \sin \mathbf{x}_3 + p_3^{(i)_j} \langle \mathbf{w}_e^{(i)_j} \rangle_r \right] \right. \\
 & \cup \left[p_1^{(k)_j} \left(v^{(k)_j} - v^{(k)_j} \cos \mathbf{x}_3^{(k)_j} \right) - p_2^{(k)_j} v^{(k)_j} \sin \mathbf{x}_3^{(k)_j} - \underline{\mathbf{w}}_p^j |p_3^{(k)_j}| \right. \\
 & \left. \left. + \tilde{\mathbf{w}}_e^j \left| p_2^{(k)_j} \mathbf{x}_1^{(k)_j} - p_1^{(k)_j} \mathbf{x}_2^{(k)_j} + p_3^{(k)_j} \right| \right] \right).
 \end{aligned} \tag{91}$$

For the special case where the linear speeds of the evading agents and pursuer are equal i.e. $v_e^{(i)_j}(t) = v_p(t) = +1m/s$, we have a murmuration's Hamiltonian as

$$\begin{aligned}
 H(\mathbf{x}, p) = & \cup_{j=1}^{n_f} \left(\cup_{i=1}^{n_a-1} \left[p_1^{(i)_j} \cos \mathbf{x}_3 + p_2^{(i)_j} \sin \mathbf{x}_3 + p_3^{(i)_j} \langle \mathbf{w}_e^{(i)_j} \rangle_r \right] \right. \\
 & \cup \left[p_1^{(k)_j} \left(1 - \cos \mathbf{x}_3^{(k)_j} \right) - p_2^{(k)_j} \sin \mathbf{x}_3^{(k)_j} - \underline{\mathbf{w}}_p^j |p_3^{(k)_j}| \right. \\
 & \left. \left. + \tilde{\mathbf{w}}_e^j \left| p_2^{(k)_j} \mathbf{x}_1^{(k)_j} - p_1^{(k)_j} \mathbf{x}_2^{(k)_j} + p_3^{(k)_j} \right| \right] \right).
 \end{aligned} \tag{92}$$

□

COROLLARY 2. *For the special case where the linear speeds of the evading agents and pursuer are equal i.e. $v_e^{(i)_j}(t) = v_p(t) = +1m/s$, we have the Hamiltonian as*

$$\begin{aligned}
 H(\mathbf{x}, p) = & \cup_{j=1}^{n_f} \left(\cup_{i=1}^{n_a-1} \left[p_1^{(i)_j} \cos \mathbf{x}_3 + p_2^{(i)_j} \sin \mathbf{x}_3 + p_3^{(i)_j} \langle \mathbf{w}_e^{(i)_j} \rangle_r \right] \right. \\
 & \cup \left[p_1^{(k)_j} \left(1 - \cos \mathbf{x}_3^{(k)_j} \right) - p_2^{(k)_j} \sin \mathbf{x}_3^{(k)_j} - \underline{\mathbf{w}}_p^j |p_3^{(k)_j}| \right. \\
 & \left. \left. + \tilde{\mathbf{w}}_e^j \left| p_2^{(k)_j} \mathbf{x}_1^{(k)_j} - p_1^{(k)_j} \mathbf{x}_2^{(k)_j} + p_3^{(k)_j} \right| \right] \right).
 \end{aligned} \tag{93}$$

We adopt the essentially non-oscillatory Lax-Friedrichs scheme of [40] in resolving (93). Denote by (x, y, z) a generic point in \mathbb{R}^3 so that given mesh sizes $\Delta x, \Delta y, \Delta z, \Delta t > 0$, letters u, v, w will represent functions on the x, y, z lattice $\Delta = \{(x_i, y_j, z_k) : i, j, k \in \mathbb{Z}\}$. We define the numerical monotone flux, $\hat{H}^{(i)j}(\cdot)$, of $H_j^{(i)}(\cdot)$ as

$$\begin{aligned} \hat{H}^{(i)j}(u^+, u^-, v^+, v^-, w^+, w^-) &= H^{(i)j} \left(\frac{u^+ + u^-}{2}, \frac{v^+ + v^-}{2}, \frac{w^+ + w^-}{2} \right) \\ &\quad - \frac{1}{2} \left[\alpha_x^{(i)j} (u^+ - u^-) + \alpha_y^{(i)j} (v^+ - v^-) + \alpha_z^{(i)j} (w^+ - w^-) \right] \end{aligned} \quad (94)$$

where

$$\alpha_x^{(i)j} = \max_{\substack{a \leq u \leq b \\ c \leq v \leq d \\ e \leq w \leq f}} |H_u^{(i)j}(\cdot)|, \quad \alpha_y^{(i)j} = \max_{\substack{a \leq u \leq b \\ c \leq v \leq d \\ e \leq w \leq f}} |H_v^{(i)j}(\cdot)|, \quad \alpha_z^{(i)j} = \max_{\substack{a \leq u \leq b \\ c \leq v \leq d \\ e \leq w \leq f}} |H_w^{(i)j}(\cdot)| \quad (95)$$

are the dissipation coefficients, controlling the level of numerical viscosity in order to realize a stable solution that is physically realistic [11]. Here, the subscripts of H are the partial derivatives w.r.t the subscript variable, and the flux, $\hat{H}(\cdot)$ is monotone for $a \leq u^\pm \leq b, c \leq v^\pm \leq d, e \leq w^\pm \leq f$. We adopt the total variation diminishing Runge-Kutta scheme of [39, 43] in efficiently calculating essentially non-oscillating upwinding finite difference gradients of $H(\cdot)$.

The computed safe sets are as shown in Figure 9. Note that the symmetry between non-consecutive flock labels e.g. flock 1 and flock 3's RCBRAT is because the we multiplied the initial position of a flock's state by -1 .

7.4 Computational Time Comparison with LevelSet Toolbox

In this subsection, we will compare the solution for recovering the zero level set of the systems presented in the previous examples against Mitchell [33]'s `LevelSet Toolbox` in MATLAB®. In all, we compare the efficacy of running various computational problems using our library on a CPU – running with Numpy and its fast arithmetic libraries versus on a CPU with MATLAB® – as originally written in Mitchell [33]'s library. In addition, we compare the efficacy of running these computational problems on a single GPU.

For the CPU tests, we run the computation on an Intel Core™i9-10885H CPU with clock frequency of 2.4GHz on 16 cores, running 62.4GB memory. We employed an NVIDIA Quadro RTX 4000 with 8.192 GiB memory running on a mobile workstation with the CPU specifications mentioned erstwhile in all of our GPU library accelerations.

Table 1 depicts the time it takes to process a full global optimization step of the reachable sets/tubes and time-to-reach sets for the examples we have considered in this work. The column `Avg. local` depicts the average time the employed method of lines for resolving the HJ PDE takes per optimization step. The column `Global` denotes the average time it takes to compute the numerical solution to the HJ PDE. We compare results of running the algorithm on a GPU, and CPU (both in Numpy and MATLAB).

On a CPU, owing to efficient arrays arithmetic native to the Harris et al. [20]'s Numpy library, the average time to compute the zero levelsets per optimization step for the `odeCFLx` functions is lower with our Numpy implementation of the Mitchell [33] `LevelSets Toolbox` library across all experiments. The inefficiencies of MATLAB®'s array processing routine in the longer time to resolve stagewise BRTs and the effective time to finish the overall HJ PDE resolution per experiment manifests in all of our experimental categories. For CPU processing of HJ PDE's, it is reasonable, based on these presented data to expect that users would find our library far more useful for everyday computations in matters relating to the numerical resolution of HJ PDE's.

Table 1. Time to Resolve Relevant HJ PDE .

Experiment	LevPy GPU Time (secs)		LevPy CPU Time (secs)		MATLAB CPU Time (secs)	
	Global	Avg. local	Global	Avg. local	Global	Avg. local
Rocket Launch	578.6729	2.9957	107.8409	10.4023	138.5000	13.8500
Double Integrator	14.7657	1.5441	3.4535	0.4317	5.2300	0.65375
Air 3D	134.7700	2.9122	312.6739	30.1073	134.7700	16.8462
Starlings flock	1276.7449	5.2129	3589.1245	15.2693	NA	NA

Similarly, across the GPU computational experiments for the examples presented, we also see that computation is significantly faster on the GPU-accelerated code for the described Air3D game of two vehicles on a plane problem as well as rocket launch differential game problem. The average local time for computing the solutions to the stagewise HJ PDE's using the method of lines for Air 3D is a gain of 90% on a GPU; the global time is a gain of 56.89% when running the algorithm on a GPU. Notice the exception with the `Double Integrator` experiment however: local and global computations take a little longer compared to deployments on the CPU – on our Harris et al. [20]'s implementation and using Mitchell [33]'s native MATLAB®toolbox. We attribute this to the little size of the arrays of interest in this problem. The entire target set of the double integral plant exists on a two-dimensional grid whose analytic and approximate time-to-reach-the-origin computational time involves little computational gain in passing data onto the GPU. Nevertheless, we still see noticeable gains in using our CPU implementations as opposed to Mitchell [33]'s native MATLAB®toolbox implementation. Therefore, the user is advised to be sacrosanct in choosing what version of our library is needful for particular computational problems involving HJ PDE's.

8 CONCLUSION

With the advent of function approximation (neural networks) and the increasing attention they are gaining in almost every domain of expertise including reinforcement learning, control systems, robotics, modeling, and real-time prediction in sensitive and safety-critical environments, it has become paramount to start considering backup safety filters for these generally unstable large function approximators in safety-critical environments. We have presented all the essential components of the python version of the LevelSetPy library for numerically resolving HJ PDEs (pertaining to the problems in the foregoing) and for advancing co-dimension one interfaces on Cartesian grids. We have motivated the work presented with several numerical examples to demonstrate the efficacy of our library.

The examples we have presented in this document provide a foray into the computational aspects of ascertaining the safety (freedom from harm) of the complex systems that we are continually designing and building. We have also looked into safe control examples encompassing complex multiagent systems whose safe navigation over a phase space can be considered in an HJ PDE environment. As complexity evolves, we hope that our library can serve as a useful tool for tinkerers looking for an easy-to-use proof-of-concept toolkit to validate ideas. We also hope that it can serve as an agent for benchmarking, verification and validation means for resolving the Hamilton-Jacobi PDE's in a principled, and guaranteed manner for users across a diverse range of fields.

We encourage users to download the library from the author's github webpage (it is available in in CPU and GPU implementations via appropriately tagged branches) and use it robustly for various problems of interest where speed and scale for the solubility of hyperbolic conservation laws and HJ PDE's are of high importance.

REFERENCES

- [1] Michael Athans and Peter L. Falb. 2013. *Optimal Control: An Introduction to the Theory and its Applications*. Courier Corporation.
- [2] M. Ballerini, N. Cabibbo, R. Candelier, A. Cavagna, E. Cisbani, I. Giardina, V. Lecomte, A. Orlandi, G. Parisi, A. Procaccini, M. Viale, and V. Zdravkovic. 2008. interaction Ruling Animal Collective Behavior Depends On Topological Rather Than Metric Distance: Evidence From A Field Study. *Proceedings of the National Academy of Sciences* 105, 4 (2008), 1232–1237. <https://doi.org/10.1073/pnas.0711437105> arXiv:<https://www.pnas.org/content/105/4/1232.full.pdf>
- [3] Tamer Basar and Geert Jan Olsder. 1999. *Dynamic Noncooperative Game Theory*. Vol. 23. Society for Industrial and Applied Mathematics.
- [4] Richard Bellman. 1957. *Dynamic programming*. Princeton University Press.
- [5] Sanjay P Bhat and Dennis S Bernstein. 1998. Continuous finite-time stabilization of the translational and rotational double integrators. *IEEE Transactions on automatic control* 43, 5 (1998), 678–682.
- [6] Burridge, R R and Rizzi, A A and Koditschek, D E. 1999. *Sequential Composition of Dynamically Dexterous Robot Behaviors*. Technical Report 6. 534–555 pages.
- [7] Andrea Cavagna, Alessio Cimorelli, Irene Giardina, Giorgio Parisi, Raffaele Santagati, Fabio Stefanini, and Massimiliano Viale. 2010. Scale-free Correlations In Starling Flocks. *Proceedings of the National Academy of Sciences* 107, 26 (2010), 11865–11870.
- [8] M. G. Crandall, L. C. Evans, and P. L. Lions. 1984. Some Properties of Viscosity Solutions of Hamilton-Jacobi Equations. *Trans. Amer. Math. Soc.* 282, 2 (1984), 487.
- [9] Michael G Crandall and Pierre-Louis Lions. 1983. Viscosity solutions of Hamilton-Jacobi equations. *Transactions of the American mathematical society* 277, 1 (1983), 1–42.
- [10] Michael G Crandall and P-L Lions. 1984. Two Approximations of Solutions of Hamilton-Jacobi Equations. *Mathematics of Computation* 43, 167 (1984), 1–19.
- [11] Michael G Crandall and Andrew Majda. 1980. Monotone Difference Approximations For Scalar Conservation Laws. *Math. Comp.* 34, 149 (1980), 1–21.
- [12] Defense Acquisition University. 2023. Validation. <https://www.dau.edu/tools/se-brainbook/Pages/Technical%20Processes/validation.aspx> Accessed April 5, 2023.
- [13] Defense Acquisition University. 2023. Verification. <https://www.dau.edu/tools/se-brainbook/Pages/Technical%20Processes/verification.aspx> Accessed April 5, 2023.
- [14] Stuart E Dreyfus. 1966. *Control Problems With Linear Dynamics, Quadratic Criterion, and Linear Terminal Constraints*. Technical Report. Rand Corp, Santa Monica Calif.
- [15] L.C. Evans and Panagiotis E. Souganidis. 1984. Differential Games And Representation Formulas For Solutions Of Hamilton-Jacobi-Isaacs Equations. *Indiana Univ. Math. J* 33, 5 (1984), 773–797.
- [16] L.C. Evans and Panagiotis E. Souganidis. 1984. Differential games and representation formulas for solutions of Hamilton-Jacobi-Isaacs equations. *Indiana Univ. Math. J* 33, 5 (1984), 773–797.
- [17] Lawrence C Evans. 2022. *Partial Differential Equations*. Vol. 19. American Mathematical Society.
- [18] Melanie Haiken. 2021. Starling murmurations are dazzling, ubiquitous, and puzzling. <https://tinyurl.com/4973byeey> Accessed April 5, 2023.
- [19] Melanie Haiken. 2021. These birds flock in mesmerizing swarms of thousands—but why is still a mystery. <https://tinyurl.com/4973byeey> Accessed April 5, 2023.
- [20] Charles R Harris, K Jarrod Millman, Stéfan J Van Der Walt, Ralf Gommers, Pauli Virtanen, David Cournapeau, Eric Wieser, Julian Taylor, Sebastian Berg, Nathaniel J Smith, et al. 2020. Array programming with NumPy. *Nature* 585, 7825 (2020), 357–362.
- [21] Dirk Helbing, Illés Farkas, and Tamas Vicsek. 2000. Simulating dynamical features of escape panic. *Nature* 407, 6803 (2000), 487–490.
- [22] Kerianne L. Hobbs, Mark L. Mote, Matthew C.L. Abate, Samuel D. Coogan, and Eric M. Feron. 2023. Runtime Assurance for Safety-Critical Systems. *IEEE Control Systems Magazine* 43 (2023), 28–65. Issue 2.
- [23] Eberhard Hopf. 1950. The Partial Differential Equation $u_t + uu_x = \mu_{xx}^*$. (1950).
- [24] R Isaacs. 1999. *Differential Games: A Mathematical Theory with Applications to Warfare and Pursuit, Control and Optimization*. Kreiger, Huntigton, NY.
- [25] Ali Jadbabaie, Jie Lin, and A Stephen Morse. 2003. Coordination of groups of mobile autonomous agents using nearest neighbor rules. *IEEE Transactions on automatic control* 48, 6 (2003), 988–1001.
- [26] Guang-Shan Jiang and Danping Peng. 2000. Weighted ENO schemes for Hamilton–Jacobi equations. *SIAM Journal on Scientific computing* 21, 6 (2000), 2126–2143.
- [27] Elia Kaufmann, Antonio Loquercio, René Ranftl, Matthias Müller, Vladlen Koltun, and Davide Scaramuzza. 2020. Deep Drone Acrobatics. *arXiv preprint arXiv:2006.05768* (2020).

- [28] S.N. Kruzkov. 1970. First Order Quasilinear Equations In Several Independent Variables. *Mathematics of the USSR-Sbornik* (1970).
- [29] Pierre-Louis Lions. 1982. *Generalized solutions of Hamilton-Jacobi equations*. Vol. 69. London Pitman.
- [30] John Lygeros. 2004. On reachability and minimum cost optimal control. *Automatica* 40, 6 (2004), 917–927.
- [31] AW Merz. 1972. The game of two identical cars. *Journal of Optimization Theory and Applications* 9, 5 (1972), 324–343.
- [32] Ian Mitchell. 2001. Games of two identical vehicles. *Dept. Aeronautics and Astronautics, Stanford Univ.* July (2001), 1–29.
- [33] Ian Mitchell. 2004. A Toolbox of Level Set Methods, version 1.0. *The University of British Columbia, UBC CS TR-2004-09* (July 2004), 1–94.
- [34] Ian Mitchell. 2020. A Robust Controlled Backward Reach Tube with (Almost) Analytic Solution for Two Dubins Cars. *EPiC Series in Computing* 74 (2020), 242–258.
- [35] Ian M. Mitchell, Alexandre M. Bayen, and Claire J. Tomlin. 2005. A Time-Dependent Hamilton-Jacobi Formulation of Reachable Sets for Continuous Dynamic Games. *IEEE Trans. Automat. Control* 50, 7 (2005), 947–957.
- [36] Ryosuke Okuta, Yuya Unno, Daisuke Nishino, Shohei Hido, and Crissman Loomis. 2017. CuPy: A NumPy-Compatible Library for NVIDIA GPU Calculations. In *Proceedings of Workshop on Machine Learning Systems (LearningSys) in The Thirty-first Annual Conference on Neural Information Processing Systems (NIPS)*.
- [37] S Osher and R Fedkiw. 2004. Level Set Methods and Dynamic Implicit Surfaces. *Applied Mechanics Reviews* 57, 3 (2004), B15–B15.
- [38] Stanley Osher and James A. Sethian. 1988. Fronts Propagating with Curvature-Dependent Speed: Algorithms based on Hamilton-Jacobi Formulations. *Journal of Computational Physics* 79, 1 (1988), 12–49.
- [39] Stanley Osher and Chi-Wang Shu. 1988. *Efficient Implementation of Essentially Non-oscillatory Shock-capturing Schemes*. Technical Report 2. Hampton, Virginia. 439–471 pages.
- [40] Stanley Osher and Chi-Wang Shu. 1991. High-Order Essentially Nonoscillatory Schemes for Hamilton-Jacobi Equations. *SIAM Journal of Numerical Analysis* 28, 4 (1991), 907–922.
- [41] James A Sethian. 1996. A Fast Marching Level Set Method For Monotonically Advancing Fronts. *Proceedings of the National Academy of Sciences* 93, 4 (1996), 1591–1595.
- [42] James A. Sethian. 2000. Level Set Methods And Fast Marching Methods: Evolving Interfaces In Computational Geometry, Fluid Mechanics, Computer Vision, And Materials Science. *Robotica* 18, 1 (2000), 89–92.
- [43] Chi-Wang Shu and Stanley Osher. 1989. Efficient Implementation of Essentially Non-oscillatory Shock-capturing Schemes, II. *Journal of computational physics* 83, 1 (1989), 32–78.
- [44] W Murray Wonham. 1985. Linear Multivariable Control: A Geometric Approach. *Applications of Mathematics* 10 (1985).

Received 10 April 2023